

Multidimensional Small Baseline Subset (MSBAS) for volcano monitoring in two dimensions: Opportunities and challenges. Case study Piton de la Fournaise volcano

Sergey V. Samsonov^{a,*}, Wanpeng Feng^a, Aline Peltier^b, Halldor Geirsson^{c,d}, Nicolas d'Oreye^{c,e}, Kristy F. Tiampo^f

^aCanada Centre for Mapping and Earth Observation, Natural Resources Canada, 560 Rochester Street, Ottawa, ON K1A0Y7, Canada

^bObservatoire Volcanologique du Piton de la Fournaise, Institut de Physique du Globe de Paris, Sorbonne Paris Cité, Univ. Paris Diderot, CNRS, F-97418 La Plaine des Cafres, La Réunion, France

^cEuropean Center for Geodynamics and Seismology, Rue Josy Welter 19, L-7256 Walferdange, Luxembourg

^dInstitute of Earth Sciences, University of Iceland, Sturlugata 7, Reykjavik 101, Iceland

^eNational Museum of Natural History, Dept. Geophysics/Astrophysics, Rue Josy Welter 19, Walferdange L-7256, Luxembourg

^fDepartment of Geological Sciences and the Cooperative Institute for Research in Environmental Sciences (CIRES), University of Colorado, Boulder, CO 80309, USA



ARTICLE INFO

Article history:

Received 7 June 2016

Received in revised form 30 March 2017

Accepted 24 April 2017

Available online 28 April 2017

Keywords:

Interferometric Synthetic Aperture Radar
InSAR

Multidimensional Small Baseline Subset
MSBAS

Ground deformation
Piton de la Fournaise
La Réunion Island

ABSTRACT

Space-borne Synthetic Aperture Radar (SAR) provides an opportunity for monitoring ground deformation at active volcanoes with high temporal and spatial resolutions. Modern SAR satellites acquire very large volumes of data that no longer can be effectively and efficiently processed and interpreted manually. The development of novel automatic processing methodologies is warranted in order to fully utilize big data. The Multidimensional Small Baseline Subset (MSBAS) methodology is an example of the semi-automatic processing system for computing temporally dense two-dimensional, horizontal east-west and vertical time series of ground deformation from ascending and descending SAR imagery acquired by various satellites. Here MSBAS is used for mapping ground deformation at the Piton de la Fournaise volcano (La Réunion Island, France) during the February 2012–April 2016 period from RADARSAT-2 data. Five volcanic eruptions occurred during the June 2014–October 2015 period, producing over 60cm of horizontal and over 30cm of vertical ground deformation, well-resolved in the MSBAS-derived time series. Validation of DInSAR results by comparison with GNSS observations and modeling of the two last and largest eruptions was performed. Validation showed good overall agreement between DInSAR and GNSS observations while revealing the benefits and limitations of both techniques. Modeling of fault and dike geometries attempted to explain the dis-proportionally large eastward motion of the eastern flank of the Piton de la Fournaise volcano that occurred during these eruptions. We demonstrated that the simple elastic model consisting of two dikes and a sliding surface can account for the observed ground deformation.

Crown Copyright © 2017 Published by Elsevier B.V. All rights reserved.

1. Introduction

Synthetic Aperture Radar (SAR) provides an opportunity for monitoring ground deformation at active volcanoes with high temporal and spatial resolutions (e.g. Samsonov et al., 2014c; Samsonov et al., 2014d; Lundgren et al., 2015a; Lundgren et al., 2015b). By combining imagery from various space-borne SAR sensors, temporally dense time series of ground deformation can be produced, complementing

Global Navigation Satellite System (GNSS) and ground-based deformation measurements. In order to effectively and efficiently utilize large volumes of SAR data, automatic processing techniques must be developed for transforming gigabytes of imagery to simple end-user friendly solutions. Because of the computational complexity, automatic processing techniques capable of this task do not yet exist. Differential Interferometric SAR (DInSAR) measures the difference in a travel time between master and slave SAR acquisitions which, in addition to ground motion, is sensitive to variations in atmospheric conditions, precision of satellite orbit determination, and variety of ground changes other than ground motion (e.g., humidity, vegetation, roughness, temperature) (Massonnet and Feigl, 1998; Rosen et al., 2000; Hooper et al., 2012). DInSAR is an established processing

* Corresponding author at: Canada Centre for Mapping and Earth Observation, Natural Resources Canada, 560 Rochester Street, Ottawa, ON K1A0Y7, Canada.

E-mail address: sergey.samsonov@nrcan.gc.ca (S.V. Samsonov).

methodology but flexibility and ambiguity in selecting some processing parameters still remains. Two main challenges of DInSAR are due to the wrapped nature of phase and the disconnection from the reference frame. Processing parameters, such as phase filter strength, coherence threshold applied during phase unwrapping, reference point location and techniques for removal of spatially and temporally correlated atmospheric noise and residual orbital trend may significantly affect the results. Various techniques have been proposed to mitigate noise components but they still remain site-specific and limited (e.g. Hanssen and Feijt, 1996; Zebker et al., 1997; Wadge et al., October, 2002; Li et al., 2005; Fournier et al., 2011; Samsonov et al., 2014d). Present day DInSAR processing is influenced by the choice of particular parameters and, therefore, not fully objective.

The Multidimensional Small Baseline Subset (MSBAS) is an advanced post-processing methodology that reconstructs two- or three-dimensional deformation time series from ascending and descending DInSAR data acquired by SAR sensors with various characteristics (e.g. wave-length, temporal and spatial resolution, imaging geometry). Temporal sampling of MSBAS results is directly proportional to the amount of DInSAR data, such that very large number of ascending and descending data sets and interferograms can be simultaneously processed to produce one set of two-dimensional deformation time series. The precision of MSBAS-derived products depends on the quality of input data (i.e. DInSAR interferograms) and can be affected by the choice of processing parameters, as those discussed above.

Previously, the MSBAS methodology has been applied to measuring ground deformation due to mining (Samsonov et al., 2013a,b, 2014), urban development (Samsonov, 2014a), carbon sequestration (Samsonov et al., 2015; Czarnogorska et al., 2016), permafrost aggradation and pingo growth (Samsonov et al., 2016), and volcanic activity (Samsonov and d'Oreye, 2012; Smets et al., 2014; Samsonov et al., 2014d; Samsonov et al., 2014c). Here we use MSBAS for studying ground deformation at the Piton de la Fournaise volcano (La Réunion Island, France) by processing ascending and descending SAR data from the Canadian RADARSAT-2 satellite. We validate the MSBAS-derived time series with GNSS time series and perform simplified numerical modeling of observed deformation. By applying the MSBAS technique to the mapping five eruptions at this volcano, we demonstrate various aspects of the methodology, which can be utilized in the next generation automatic processing system used for volcano monitoring. Availability of DInSAR data necessitates the development of new processing methodologies. The approach proposed here produces temporally dense time series, which are better suited for an advanced analysis. Geophysical modeling can be as easily carried out on ascending and descending data directly, but modeling outcomes depend on selection of the initial model parameters, such as fault locations and type of deformation. Knowledge of vertical and horizontal components can help select the appropriate initial model parameters.

Piton de la Fournaise (Fig. 1) is an active hot-spot basaltic volcano located on La Réunion Island (France) east of Madagascar in the south-west Indian Ocean. With a mean of 2.6 eruptions per year during the 1998–2011 period (e.g. Peltier et al., 2009; Roult et al., 2012; Staudacher et al., 2015), it is considered one of the most active volcanoes in the world. Since the establishment of the volcano observatory (Observatoire Volcanologique du Piton de la Fournaise - OVPF/IPGP) in 1980, eruptive activity is described as discrete events – 20 days duration on average and often $<20 \times 10^6 \text{ m}^3$ of product emitted to the surface – displaying mainly effusive activity with lava fountaining and lava flow emplacement. Each eruption is preceded by precursors (edifice inflation, increase of volcano-tectonic seismicity, degassing) occurring on two distinct time scales: low intensity at the scale of the plumbing system pressurization (from weeks to months) and strong intensity at the scale of the dike propagation to the surface (from minutes to tens of hours, (Peltier et al., 2009)).

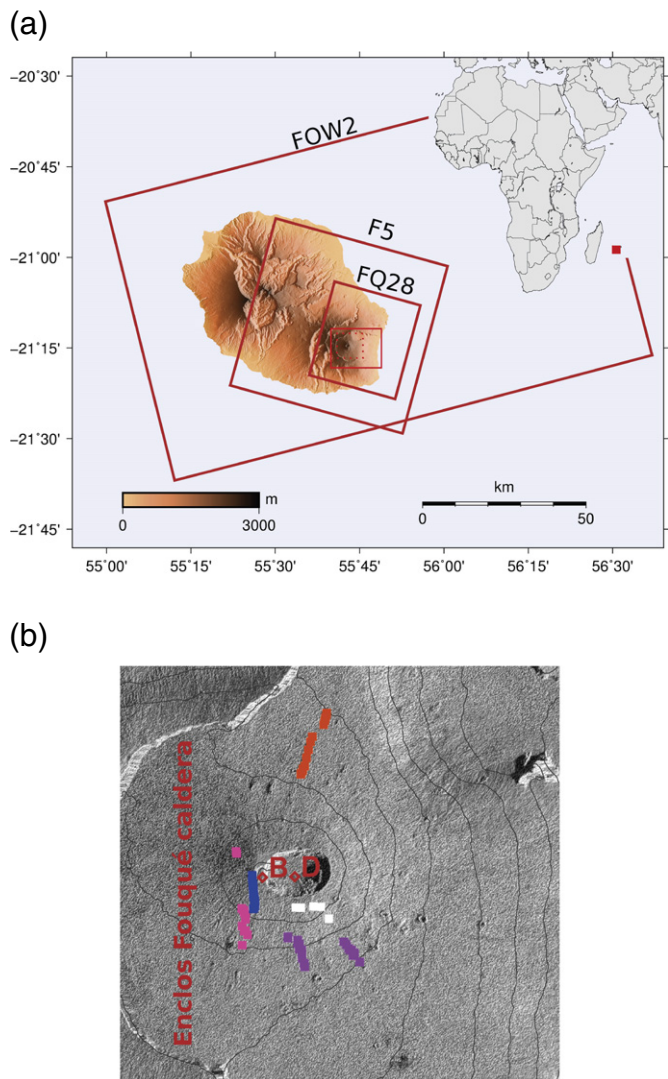


Fig. 1. (a) Shuttle Radar Topography Mission Digital Elevation Model (SRTM DEM) of La Réunion Island (France) located east of Madagascar in south-west Indian Ocean (see inset in top-right corner). Ascending and descending RADARSAT-2 frames are outlined in brown. Location of study site, i.e. Enclos Fouqué caldera of Piton de la Fournaise, is outlined in solid red. Region, for which deformation time series maps are shown below is outlined in dotted red. (b) Average intensity of F5 beam for dotted in (a) region. Eruptive fissures are shown as colored segments (Peltier et al., 2016) : June 20–21, 2014 (white), February 4–15, 2015 (blue), May 17–30, 2015 (violet), July 31–August 2, 2015 (orange), August 24–October 31, 2015 (pink). D and B refer to Dolomieu and Bory craters.

After an unusual period of rest and edifice deflation of 41 months, the OVPF monitoring network recorded first signs of reawakening on June 9, 2014 with the resumption of the edifice inflation (Peltier et al., 2016). Five eruptions followed the initial unrest (see Fig. 1 (b) for locations): (1) June 20–21, 2014 (south-southeast of the Dolomieu crater, $0.4 \pm 0.2 \times 10^6 \text{ m}^3$ of erupted products (Peltier et al., 2016)), (2) February 4–15, 2015 (west-southwest of the Bory crater, $1.5 \pm 0.2 \times 10^6 \text{ m}^3$), (3) May 17–30, 2015 (to the south-southeast, $4.6 \pm 0.6 \times 10^6 \text{ m}^3$), (4) July 31–August 2, 2015 (to the north, $2.0 \pm 0.3 \times 10^6 \text{ m}^3$), (5) and August 24–October 31, 2015 (to the west-southwest with 3 successive stages: August 24–October 18, October 22–24, and October 29–31, $35.7 \pm 3.0 \times 10^6 \text{ m}^3$). Each of these eruptions occurred inside the about $8 \times 13 \text{ km}$ wide Enclos Fouqué caldera (Fig. 1 (b)), which is a structure formed 4500 years ago (Bachèlery, 1981), and inside which the terminal cone formed. These

Table 1

SAR data sets used in this study: RADARSAT-2 ascending Fine Wide (FOW2), descending Fine (F5) and descending Fine Quad-Pol (FQ28); time span (in YYYYMMDD format), azimuth θ and incidence ϕ angles, number of available SAR images N , and number of calculated interferograms M for each data set.

InSAR set	Time span	θ°	ϕ°	N	M
R2-FOW2 (asc)	20120211–20160402	346	36	30	162
R2-F5 (dsc)	20110908–20160414	–165	47	27	118
R2-FQ28 (dsc)	20140519–20150701	–165	47	9	33
Total	20120211–20160402			64	313

five eruptions displayed activity typically observed at this volcano, i.e. early activity was characterized by the opening of an-echelon fissures from which lava fountains and flows were ejected. The lava focused in the lowest fissure the following days, leading to the edification of an eruptive cone.

Based on surface deformation recorded by the permanent GNSS stations, Peltier et al. (2016) evidenced deep fluid transfer during this period with an increased rate during mid-April 2015, a period during which deep seismicity was recorded (Lengliné et al., 2016). During that time, the pre- and inter-eruptive periods were characterized by a long-term nearly continuous edifice inflation whose pressure sources (fluid accumulation), deduced from simple Mogi sources (Mogi, 1958), ranged from 3.9 to 1.2–1.7 km depth (Peltier et al., 2016). The shallowest depths correspond to a level of shallow magma accumulation, from which the dikes initiated to feed the eruptions at the surface.

2. Differential Interferometric Synthetic Aperture Radar (DInSAR) data and methodology

We collected SAR data during September 2011–April 2016 SAR in Single Look Complex (SLC) format from one ascending Fine Wide (FOW2) and two descending Fine (F5) and Fine Quad-Pol (FQ28) RADARSAT-2 sets (Table 1, Fig. 1 (a)). Each SAR data set was processed independently with the GAMMA software (Wegmüller and Werner, 1997) in the following way. A single master for each set was selected and the remaining images were re-sampled into the master geometry. The spatially averaged (i.e. multilooked, 1 in range and 2 in azimuth) interferograms were computed and the topographic phase was removed using the 30 m resolution Shuttle Radar Topography Mission (SRTM) Digital Elevation Model (DEM). Differential interferograms were filtered using the adaptive filtering with a filtering function based on local fringe spectrum (Goldstein and Werner, 1998) and unwrapped using the minimum cost flow algorithm (Costantini, 1998). The residual orbital ramp was observed in many interferograms and baseline refinement was performed to correct it. For this, the area experiencing large ground deformation was masked out and a procedure implemented in GAMMA software that re-estimates baseline parameters based on the measurement of interferometric phase and topographic height was applied. The topography-dependent part of the atmospheric signal was also removed by this procedure because of the favorable configuration. The eastern flank of the volcano has gradually increasing topography that covers a large part of the imaged area. Therefore the topography-dependent atmospheric signal in this area resembles an east-west trend, indistinguishable from the orbital ramps.

Minor interpolation of each interferogram was performed in order to improve the spatial coverage reduced by decorrelation. This process is described in greater detail in Samsonov et al. (2011a). Then, ascending and descending interferograms were geocoded and resampled to a common lat/long grid for a reduced spatial extent that covers only the study area with the uniform spatial sampling

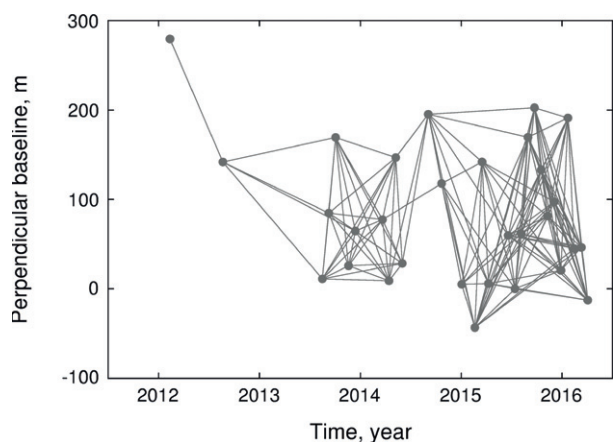
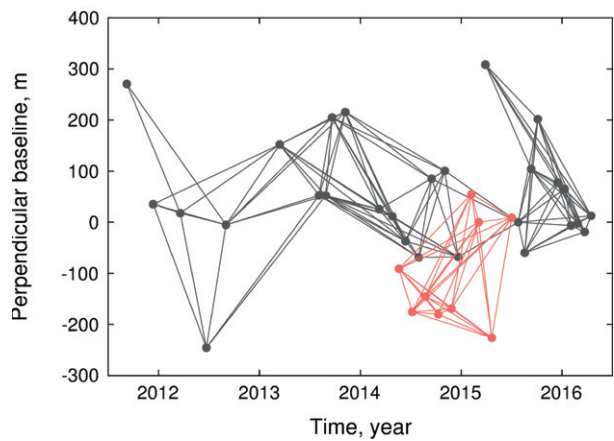
(a) Ascending R2-FOW2**(b) Descending R2-F5 and R2-FQ28 (dsc)**

Fig. 2. Perpendicular baseline and time span of automatically selected ascending R2-FOW2 (black) (a) and descending R2-F5 and R2-FQ28 (red) (b) interferograms used in this study.

of 10 m, using GMT¹ scripts. For time series analysis we selected 313 highly coherent interferograms with an average coherence after filtering (computed over common reference area) above 0.75: 162 from FOW2, 118 from F5, and 33 from FQ28 beams (Table 1). The interferometric coherence largely depends on the length of spatial and temporal baselines (Fig. 2). The spatial baseline is a distance between satellite passes and the temporal baseline is a duration of time between satellite passes. Interferometric coherence is inversely proportional to baseline lengths, i.e. short spatial and temporal baselines usually produce highly coherent interferograms. Sometimes, however, longer temporal baseline interferograms are coherent due to favorable seasonal effects.

The Multidimensional Small Baseline Subset (MSBAS) technique was applied to compute the two dimensional vertical and horizontal east-west deformation time series from overlapped in time and space ascending and descending DInSAR data:

$$\begin{pmatrix} \hat{A} \\ \lambda L \end{pmatrix} \begin{pmatrix} V_E \\ V_U \end{pmatrix} = \begin{pmatrix} \hat{\Phi} \\ 0 \end{pmatrix} \quad (1)$$

¹ <http://gmt.soest.hawaii.edu/>.

where matrix $\hat{A} = \{s_E A, s_U A\}$ consists of time intervals between consecutive SAR acquisitions A (for example of A see Samsonov (2010)) and east and up components of a line-of-sight vector $s = \{s_E, s_U\} = \{-\cos\theta\sin\phi, \cos\phi\}$, θ is azimuth and ϕ is incidence angles, V_E and V_U represent unknown horizontal east-west and vertical velocities that are to be determined, $\hat{\Phi}$ represents observed DInSAR data, geocoded and resampled to a common grid, λ is a regularization parameter and L is a zero, first, or second order difference operator. Thus, MSBAS software computes vertical and horizontal deformation rates between consecutive acquisitions V_E and V_U for each pixel by simultaneously processing ascending and descending DInSAR data. Deformation time series are reconstructed from the computed deformation rates by numerical integration.

The choice of regularization order depends on the signal characteristics and study objectives. In case of the zero order regularization the solution is found by least square fitting of data and by minimizing the solution norm (i.e. deformation rates between consecutive acquisitions V_E and V_U). This type of regularization should be used when the mean of the deformation rates is expected to be close to zero (e.g. oscillating motion). If such methodology is used for describing a steady motion then the solved deformation rates will likely be smaller than the actual due to the bias introduced by minimization of the solution norm.

In case of the first and second order regularizations, the solution is found by least square fitting of data and by minimizing the first and second differences between consecutive in time deformation rates.

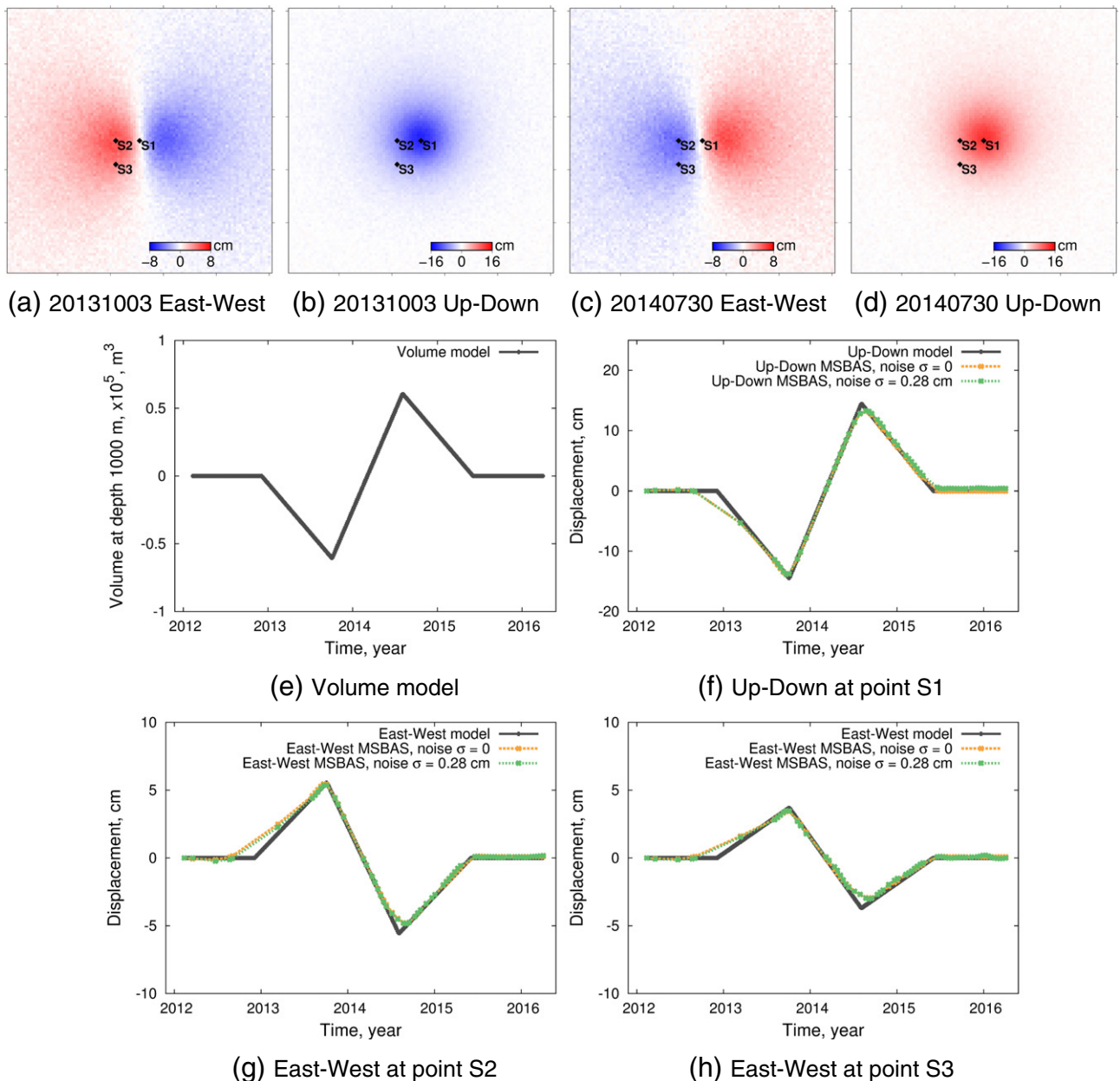


Fig. 3. Spatial and temporal resolution tests. Reconstructed with MSBAS horizontal east-west and vertical cumulative deformation (7500×7500 m) maps during 20120211–201131003 (a–b) and 20120211–20140730 (c–d) due to Mogi point source located at 1000 m depth and with volume varying according to (e). At points S1–S3 time series of cumulative deformation were extracted: vertical modeled and reconstructed time series at point S1 (f); horizontal east-west modeled and reconstructed cumulative time series at points S2 (g) and S3 (h). Two sets of synthetic DInSAR data were produced: without noise (yellow) and with noise $\sigma = 0.28$ cm (green). Note that observations are marked with points, interpolated lines are plotted for clarity only.

This approach is suitable for mapping oscillating and steady motions. The first order regularization was used here.

Previous versions of SBAS (Samsonov et al., 2011b) and MSBAS were capable of performing spatial high- and low-pass filtering and temporal Gaussian smoothing. This functionality was removed from the current version of MSBAS software as the spatial filtering can be more accurately performed prior to MSBAS processing with external software (e.g. GMT) and temporal smoothing is produced by regularization. The strength of temporal smoothing is controlled by the regularization parameter λ Eq. (1) and the optimal value can be

chosen, for example, with the L-curve method (Hansen and O'Leary, 1993).

Selection of the reference point deserves particular attention. It needs to be selected in a stable region, located not far away from the studied area, since the DInSAR precision is inversely proportional to the distance between reference and measured regions. Reduction of precision with distance is due to residual orbital ramps and atmospheric signals remaining in interferograms. In Samsonov et al. (2014c) we demonstrated that about 50% of the atmospheric signal can be explained by the predictable seasonal variability of

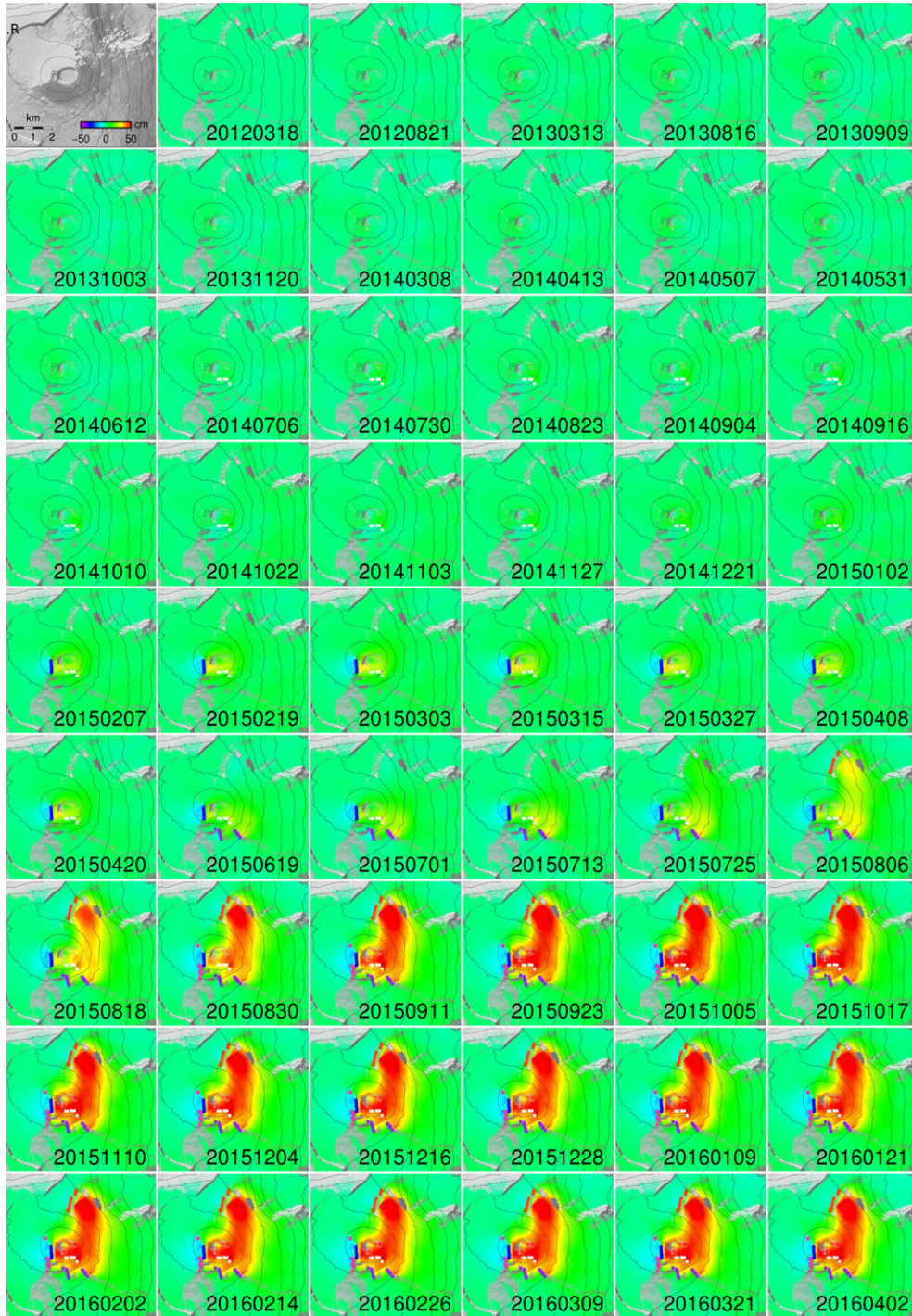


Fig. 4. Time series of cumulative horizontal east-west deformation computed with MSBAS during 20120211–20160402. Eruptive fissures are shown as segments: June 20–21, 2014 (white), February 4–15, 2015 (blue), May 17–30, 2015 (violet), July 31–August 2, 2015 (orange), August 24–October 31, 2015 (pink).

temperature, pressure and humidity in the low troposphere. We demonstrated that in order to reduce this noise component the reference point must be chosen at the same altitude as the measured area. Here it was possible to achieve this by selecting reference point right outside of Enclos Fouqué caldera, close to GITG GNSS site.

3. Numerical simulation

Because the quality of the MSBAS results depends on the quality and quantity of DInSAR data, spatial and temporal resolution tests

(Fig. 3) were performed with the actual time-geometry matrix \hat{A} (i.e. actual number of data sets, interferograms in each set and acquisition and temporal characteristics). As input signal, we simulated three-dimensional ground deformation due to the Mogi source (Mogi, 1958; Tiampo et al., 2004) located at a depth of 1000 m with the volume changing according to Fig. 3 (e) and computed synthetic interferograms due to this source, similar to those in Table 1 and Fig. 2. The entire time span was divided into five equal intervals. During the first and last intervals there was no volume change; during the second and fourth intervals there was reduction in volume;

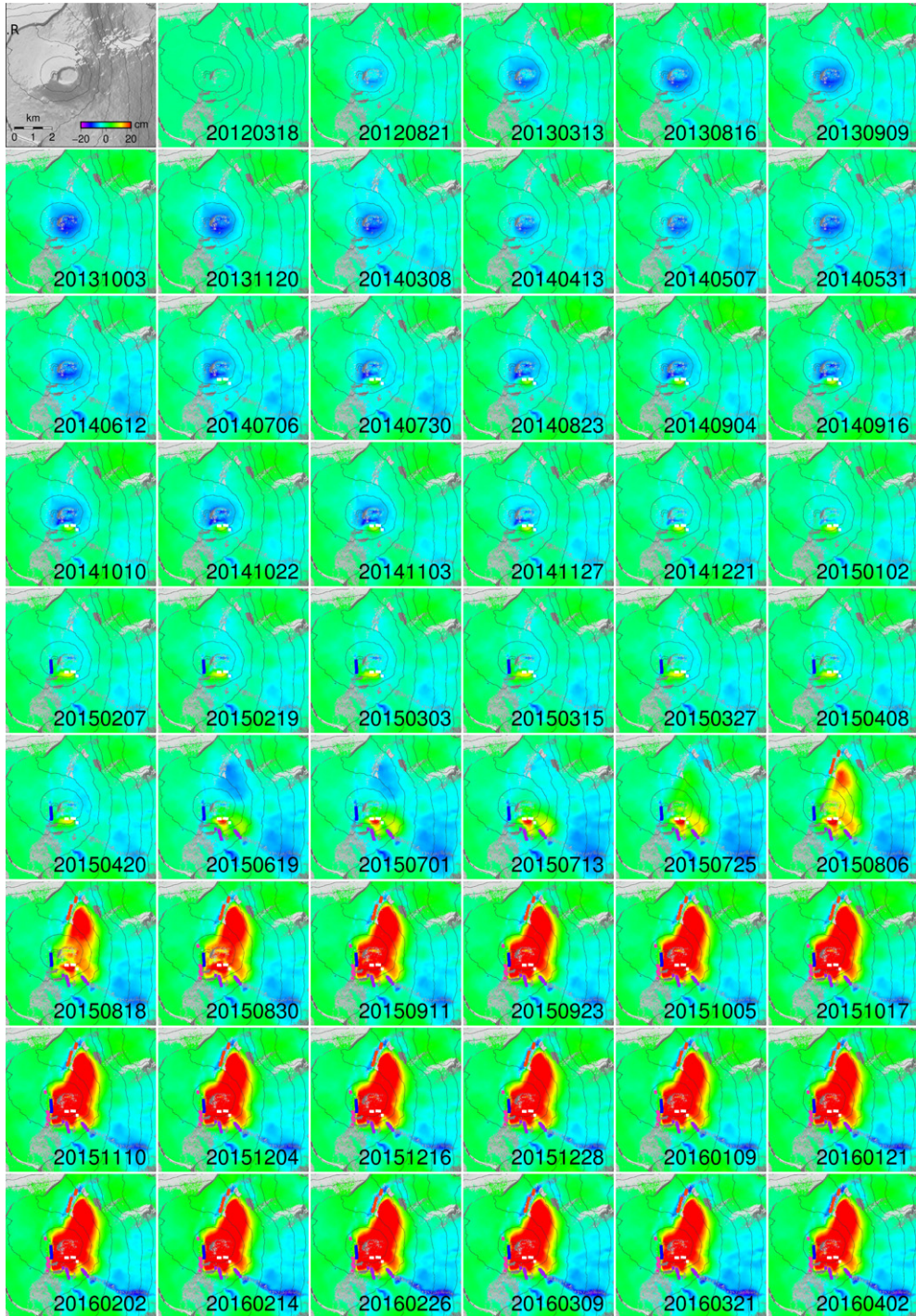


Fig. 5. Time series of cumulative vertical deformation computed with MSBAS during 20120211–20160402. Eruptive fissures are shown as segments: June 20–21, 2014 (white), February 4–15, 2015 (blue), May 17–30, 2015 (violet), July 31–August 2, 2015 (orange), August 24–October 31, 2015 (pink).

and during the third interval there was an increase in volume (Fig. 3 (e)). The simulation was performed for two cases: without noise and with added white noise with standard deviation of 0.28 cm (1/10 of fringe).

The vertical and horizontal east-west cumulative deformation maps reconstructed with MSBAS are shown in Fig. 3 (a)–(d) for time steps, at which magnitude of deformation is largest. Additionally, time series at three points, S1–S3, are shown in separate plots. Point S1 is located right above the source and it experiences only vertical motion shown in Fig. 3 (f). Point S2 is located west of the source, where the northern component is equal to zero and the eastern component is largest. For this point only the east-west time series are shown. Point S3 is located south-west of the source and it experiences both northern and eastward motion of equal magnitude.

As expected, the quality of reconstruction of the vertical component of the displacement is slightly better than that of the horizontal east-west component and the distortion due to the unaccounted north-south component in the observed components is minor. These results show that the current data set (defined by matrix \hat{A}) can be successfully used for reconstruction of two-dimensional deformation time series using MSBAS methodology.

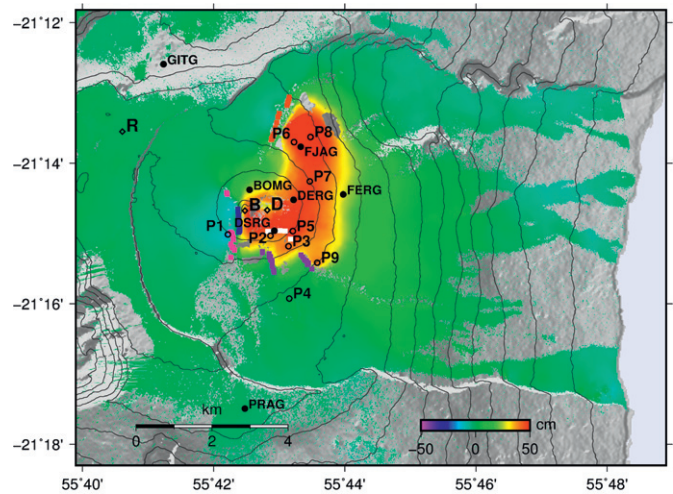
4. Results

The two-dimensional deformation time series computed with MSBAS are shown as cumulative deformation maps in order to better demonstrate the spatial extent of the deformation. The individual time series for selected points also are shown in order to better demonstrate the temporal pattern of deformation. The cumulative horizontal east-west deformation maps are shown in Fig. 4, the color scale is set to ± 50 cm and large values are saturated. The cumulative vertical deformation maps are shown in Fig. 5, the color scale is set to ± 20 cm and large values are also saturated. Deformation maps for a larger region at the final epoch of 20160402 are shown in Fig. 6, along with the GNSS sites discussed below in the paper and five eruptive fissures of the studied period. The time series for nine points P1–P9, selected at locations of local extreme deformation values, are shown in Fig. 7.

Prior to the first eruption on June 20–21, 2014 (white fissure in Fig. 6, south-southeast of Dolomieu crater, $0.4 \pm 0.2 \times 10^6$ m 3 of erupted products (Peltier et al., 2016)) only minor subsidence was observed around the summit of the volcano (Fig. 5, e.g. Fig. 7 (b)–(e)). The MSBAS results show that rapid motion began after the first eruption, observed as uplift at P2 (Fig. 7 (b)) and horizontal at P3, P5, P7 (Fig. 7 (c), (e), (g)). Eastward motion at P7 suggests broader instability of the eastern flank. Fast motion continued for a few months and then slowed. Rapid horizontal motion at P1 (Fig. 7 (a)) started a few months prior to the second eruption on February 4–15, 2015 (blue fissure in Fig. 6, west-southwest of Bory crater, $1.5 \pm 0.2 \times 10^6$ m 3), followed by the overall decrease in deformation activity. Smaller motion observed at other points (e.g. P2, P3) can be attributed to over-smoothing caused by regularization. The third eruption on May 17–30, 2015 (violet fissure in Fig. 6, to the southeast, $4.6 \pm 0.6 \times 10^6$ m 3) produced ground deformation at points P2–P5, P9 (Fig. 7 (b)–(e), (i)). The fourth eruption on July 31–August 2, 2015 (orange fissure in Fig. 6, to the north, $2 \pm 0.3 \times 10^6$ m 3) and the fifth eruption on August 24–October 31, 2015 (pink fissure in Fig. 6, to the west-southwest, $35.7 \pm 3 \times 10^6$ m 3) produced largest deformation observed at all nine points P1–P9 (Fig. 7). Maximum uplift produced by the last two eruptions reached approximately 40 cm at P6 (Fig. 7 (f)) and horizontal motion reached over 60 cm at P5, P8 (Fig. 7 (e), (h)). The size of the deformed area reached about 2×4 km in east-west and north-south directions, respectively.

In addition to co-eruptive deformation, subsidence was observed at a few remote areas (e.g. south-east of P4, P9 and near the coast

(a) Horizontal east-west



(b) Vertical

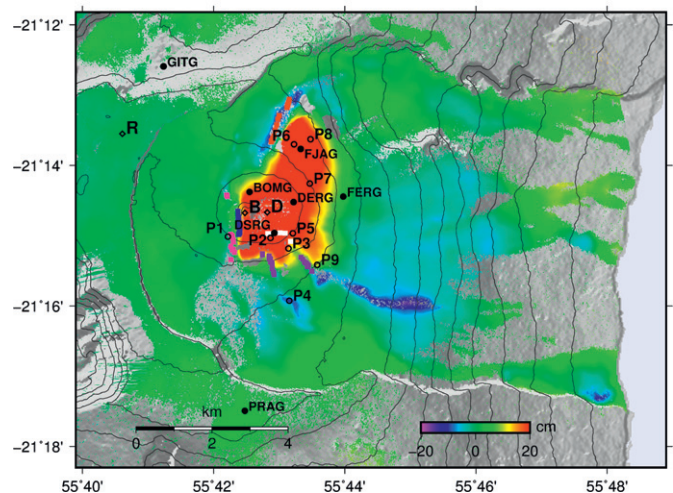


Fig. 6. Cumulative horizontal east-west (a) and vertical (b) ground deformation during 2012011–20160402, computed with MSBAS. Location of GNSS sites are shown as black filled circles, location of points P1–P9, at which local extreme deformation values were observed are shown as black empty circles. R is reference point for MSBAS analysis, D is Dolomieu and B is Bory craters. Eruptive fissures are shown as segments: June 20–21, 2014 (white), February 4–15, 2015 (blue), May 17–30, 2015 (violet), July 31–August 2, 2015 (orange), August 24–October 31, 2015 (pink).

(Fig. 6 (b))), likely caused by compaction and cooling of recent surface lava flows and deposits.

5. Comparison with observations from Global Navigation Satellite System (GNSS)

OVPF maintains a GNSS network composed of 24 stations covering both the active terminal cone, the sliding eastern flank and the less active parts located outside of the Enclos Fouqué caldera. The receivers are 15 Topcon GB1000, 3 Trimble NetRS, and 6 Trimble NetR9, all of which have a sampling rate of 30 s. Data files are transmitted to OVPF by long-range Wi-Fi, and daily solutions are automatically processed at the observatory with the GAMIT/GLOBK software package (Herring and King, 2010). We use (i) international

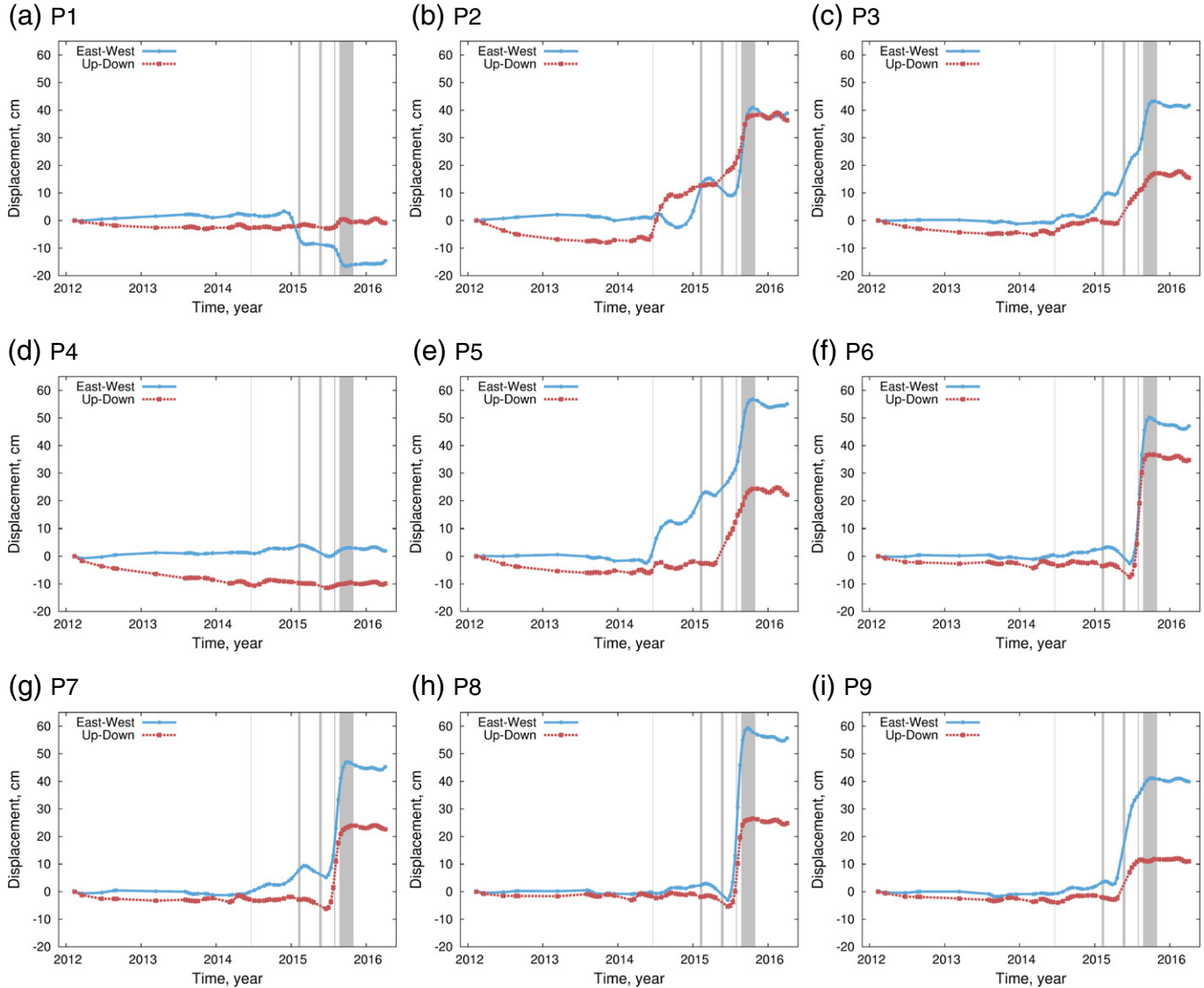


Fig. 7. Horizontal east-west and vertical time series of ground deformation during 20120606–20150816 for points P1–P9 from Fig. 6 computed with MSBAS. Time of eruptions are marked as gray rectangles.

GNSS Service (IGS) precise ephemerides; (ii) a stable support network of 20 IGS stations off La Réunion Island scattered around the Indian Ocean Islands and coasts; (iii) a tested parameterisation of the troposphere; and (iv) models of ocean loading, Earth and lunar tides. For a better comparison with the DInSAR data from this study, all GNSS data are referenced to GITG, located close to the reference point used for MSBAS analysis.

The MSBAS-derived deformation time series were compared with GNSS time series observed at five sites: FJAG, BOMG, FERG, DERG, and DSRG (Fig. 8). Overall agreement between DInSAR and GNSS measurements is very good at four sites in term of intensity, but small delay is observed in DInSAR time series due to smoothing by regularization. Indeed, the rapid ground deformation was recorded during the dike propagation to the surface, during a few minutes/hours preceding the eruption and not after the eruption onset as observed on MSBAS in June 2014. Very slow, long-term drift is observed in the DInSAR time series prior to 2014, which can be explained by the sparse temporal resolution during this period (Fig. 2) and also by a difference in reference frames. Agreement over the entire time span, including short term co-eruptive deformation, is good. This is

consistent with Peltier et al. (2017) results, who found for the 2015 eruptions, most of the GNSS-InSAR residuals <2.5 cm and <5 cm in the EW and vertical components, respectively, i.e. within the error bar of each method.

However, a very large discrepancy in vertical component is observed at DSRG during the first eruption on June 20–21, 2014. During this time GNSS experienced over 30 cm of subsidence but the DInSAR experienced over 10 cm of uplift. In order to understand this discrepancy in Fig. 8 (f)–(g) we plotted wrapped DInSAR interferograms spanning this event, along with GNSS site location. Site DSRG is at the edge of the coherent and regularly deforming region in Fig. 8 (f)–(g). Indeed, the eruptive fissure was observed to open a few meters south of DSRG, confirming that the subsiding tip of the dike would pass very close below the station. Thus this discrepancy is caused by a highly localized deformation field that is not well captured by the DInSAR images and is not observed at other GNSS sites.

It is apparent from the GNSS results that deformation pattern consists of a few instantaneous and large deformation due to dike injection and slow and small inter-eruptive deformation. The MSBAS

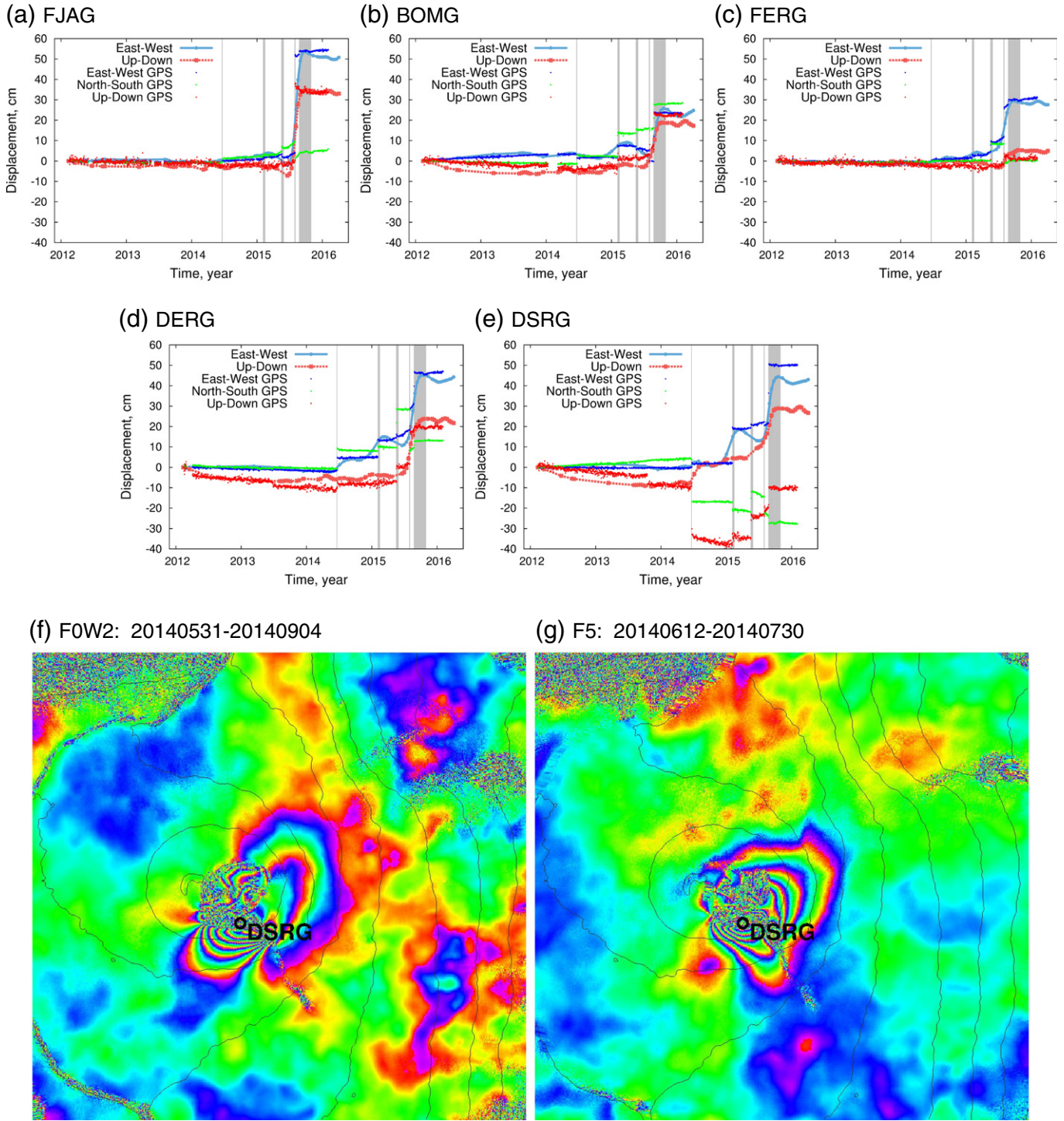


Fig. 8. Horizontal east-west and vertical time series of ground deformation computed with MSBAS during 20120606–20150816 for GNSS site locations: FJAG (a), BOMG (b), FERG (c), DERG (d), DSRG (e) (see Fig. 6). For better comparison with DInSAR, all GNSS data are referenced to GITG. Components are colored in the following way: DInSAR EW – light blue, DInSAR UD – light red, GPS NS – green, GPS EW – blue, GPS UD – red. Time of eruptions are marked as gray rectangles. Wrapped interferograms spanning the first eruption during June 20–21, 2014 (f–g) that produced over 40 cm of subsidence at DSRG site location. Due to very large phase gradient this deformation is not detected in interferograms.

deformation pattern appears gradual because of the sparse temporal sampling of SAR data and applied regularization. The smoothing effect of regularization can be observed in Fig. 9 that shows east-west component of MSBAS-derived time series observed at DERG site, similar to Fig. 8 (d). The first order regularization with λ equal to 0.1 seems optimal, causing the lag equal to approximately 0.5–1

interval of repeat cycle (RADARSAT-2: 12–24 days). Therefore, when we refer to fast deformation in MSBAS results we compare to different periods of time series and not to GNSS results. The choice of regularization parameter depends on the nature of deformation pattern. For slow (relative to observation repeat cycle) deformation large values of regularization parameter λ may work well but for

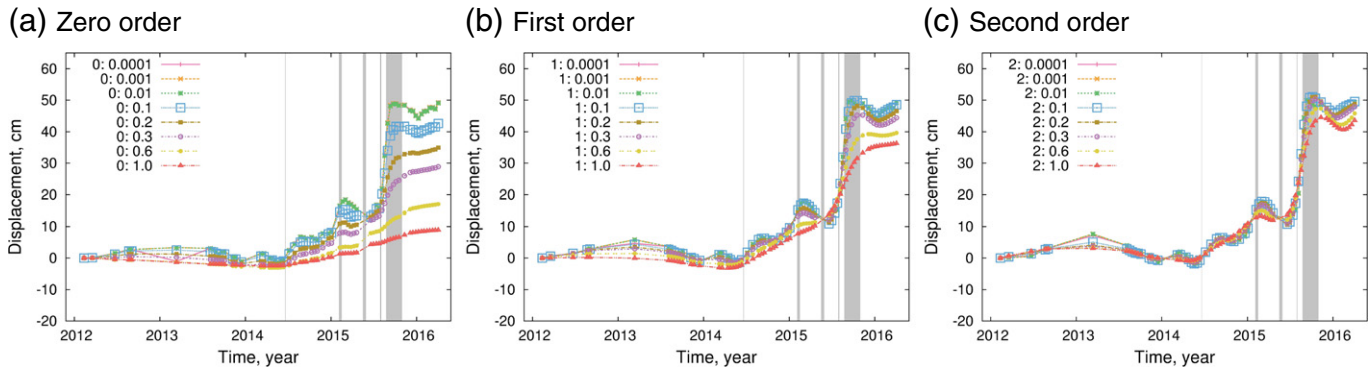


Fig. 9. MSBAS-derived east-west component observed near DERG site (Fig. 8 (d)). Smoothing effect due to zero, first and second order regularizations for different regularization parameters λ in range 0.0001–1.0; $\lambda = 0.1$ was used in this study. Time of eruptions are marked as gray rectangles.

fast or nearly-instantaneous deformation the regularization parameter λ should be chosen sufficiently small in order to minimize the lag. For testing purposes before applying MSBAS to all sets it is recommended to apply the SBAS technique to each individual set to assess the temporal variability of deformation and to guide the selection of regularization type and value of λ .

6. Interpretation and modeling

According to DInSAR results the two last diking events of July 31 and August 24, 2015 produced largest ground deformation (Figs. 4–7) and only these two events were studied here in more details. The cumulative deformation during 20150619–20160109 was computed by subtracting from the 20160109 horizontal east-west and vertical deformation maps the 20150619 deformation maps, resulting in deformation occurring during 20150619–20160109. Both horizontal east-west and vertical components were considered in modeling.

Several theoretical physical mechanisms, e.g. simple point source (Mogi source), sill and dike models can reproduce surface deformation due to volcanic activities (Dzurisin, 2006). Here we derived three models of increased complexity based on the Okada (1985) elastic half-space dislocation theory. The dike and fault planes were discretized with a depth-dependent algorithm within given dimensions (Table 2). The inversion was performed with the PSOKINV geodetic inversion package (Feng et al., 2014) utilizing the bounded least square algorithm (Ward and Barrientos, 1986).

6.1. Model 1

This model assumed opening of two dikes D1 and D2, which locations at the surface were fixed based on the DInSAR observations (Fig. 10). Opening of the dikes x was estimated by solving a linear problem, $Gx = D$, where G is the Green's function, D is the DInSAR observations, including vertical and horizontal east-west components. To reduce large variations between adjacent patches, a two-dimensional Laplacian operator was applied in the above equation (Parker, 1994). In order to calculate G , we used an elastic half-space dislocation model (Okada, 1985), where only fault opening was considered and variation of surface topography was ignored. To exclude potential plastic deformation (Griffiths, 2000) presented in horizontal east-west component (discussed below), we gave the priority to the vertical component with relative weights of 10 to 1. For estimating optimal dip angles, we iterated dip angles from 5° to 85° with a step of 5° for the both dikes.

The dikes, produced by this mode, have dip angles of $50 \pm 10^\circ$, which is consistent with the estimations of $50\text{--}70^\circ$ for previous

events (Froger et al., 2004; Fukushima et al., 2005; Peltier et al., 2008; Fukushima et al., 2010). The dike models with dip angle $> 60^\circ$ produce significant deformation west of the Enclos Fouqué caldera that is not observed in this study. The total volume change during the 20150609–20160109 period is $2.9 \times 10^6 \text{ m}^3$ and the maximum opening is 2.3 m (Table 2, Fig. 11). The predicted vertical deformation is in good agreement with the observations (Fig. 10 (f)), in which the standard deviation of residuals along the two profiles A-B and C-D are only 1.3 and 1.5 cm, respectively (Table 3, Fig. 12). However, only 50% of horizontal east-west motion can be predicted (Figs. 10 (c), 12), indicating the presence of other processes during studied period.

6.2. Model 2

Attempting to better describe horizontal east-west deformation, in this model we allowed a dip-slip in addition to opening on the two dikes D1 and D2 (Fig. 13), with similar locations at the surface as in Model 1. During the inversion, equal weights were assigned to both components of deformation. Differing from Model 1, the iteration of dip angles in Model 2 was performed separately.

The dikes, produced by this mode, have dip angles of $30 \pm 10^\circ$ for D1 and $24 \pm 10^\circ$ for D2. The total volume change during the 20150609–20160109 period is $3.0 \times 10^6 \text{ m}^3$, the maximum opening

Table 2

Deduced model parameters for models 1–3 from Figs. 10–17. D1 and D2 are dikes, and N1 is normal fault.

	Parameters	D1	D2	N1
Model 1	Length, km	2.2	3.5	5
	Width, km	3.2	3.2	4.9
	Top depth, km	0	0	0
	Bottom depth, km	2.46	2.46	1.27
	Number of patches	196	152	416
	Patch size	Variable	Variable	Variable
	Dip, $^\circ$	50 ± 10	50 ± 10	–
Model 2	Max opening, m	2.3	–	–
	Volume $\times 10^6, \text{m}^3$	2.9	–	–
	Dip, $^\circ$	30 ± 10	24 ± 10	–
	Max opening, m	1.6	–	–
Model 3	Max slip, m	1.3	–	–
	Volume $\times 10^6, \text{m}^3$	3.0	–	–
	Dip, $^\circ$	50 ± 10	50 ± 10	15 ± 5
	Max opening, m	3.2	–	–
	Max slip, m	–	0.7	–
	Volume $\times 10^6, \text{m}^3$	3.6	–	–

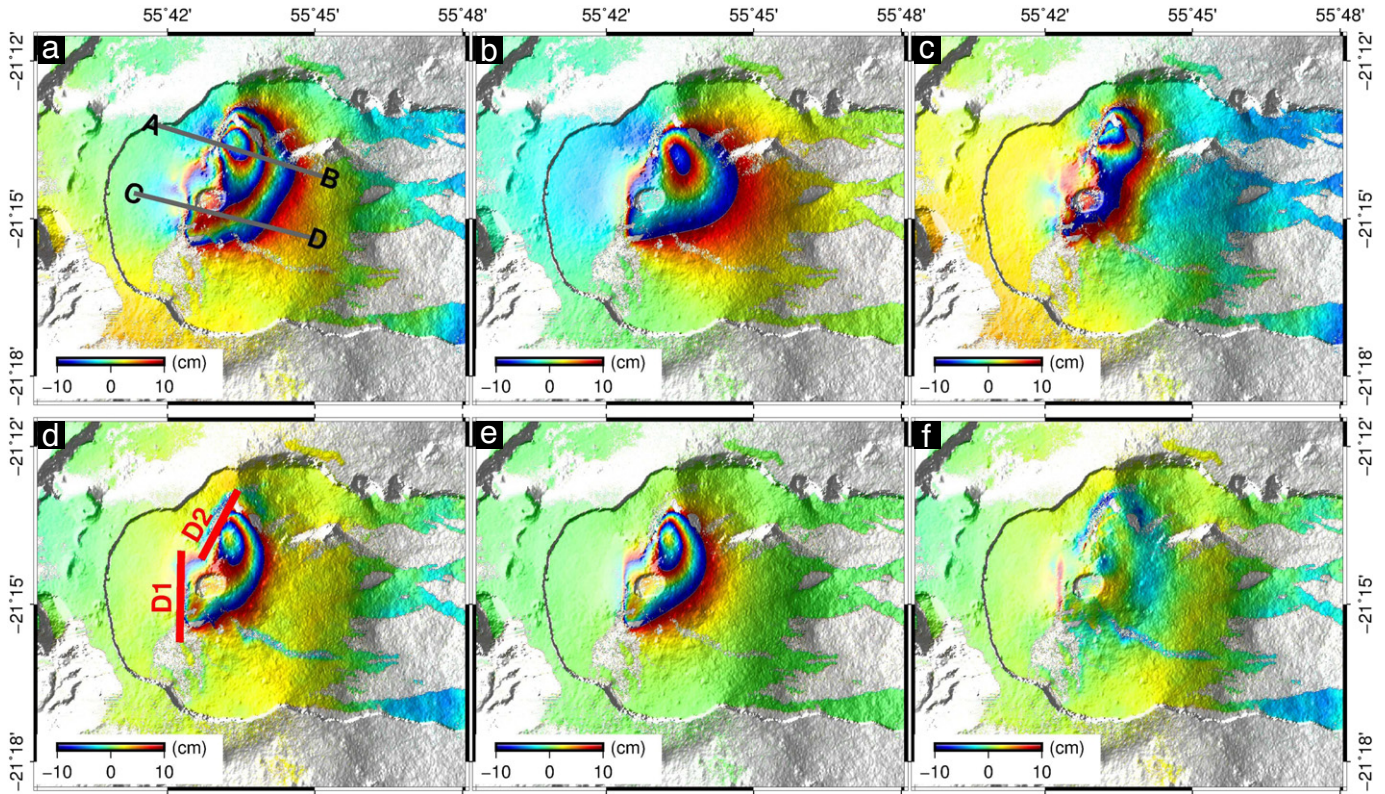


Fig. 10. Model 1 (two dikes D1–D2, opening only): horizontal east-west observed, modeled and residual deformation occurred during 20150619–20160109 (top row, a–c) and vertical observed, modeled and residual deformation during same time (bottom row, d–f). D1 and D2 are locations of modeled dikes at surface. A–B and C–D are profiles used for evaluating quality of modeling.

is 1.6 m and the maximum slip is 1.3 m (Table 2, Fig. 14). The predicted vertical and horizontal east-west deformation with the best-fitting dikes is in good agreement with the observations (Fig. 13), in which the standard deviation of residuals along the two profiles A–B and C–D are only 4.4 and 3.7 cm for vertical component and 1.7 and 1.8 cm for horizontal east-west component, respectively (Table 3, Fig. 15). This model produces shallower-dipping dikes than predicted in the previous studies and the fit of the vertical component is worse than in Model 1.

6.3. Model 3

In order to account for the large residuals in the horizontal east-west component observed in Model 1 (Fig. 10 (c)), in this model

we introduced, in addition to two dikes D1 and D2 experiencing opening, a normal fault N1 experiencing dip-slip representative of sliding process. Normal faulting events caused by the complex interactions between tectonics, magma intrusions and gravity are known to accompany volcanic activities (Froger et al., 2004; Day et al., 1999; Cianetti et al., 2012; Denlinger and Morgan, 2014). The surface location of N1 was fixed based on the residuals of the horizontal east-west component in Model 1 (Fig. 10 (c)), which is almost parallel with D2. The Green's function of the dip-slip was computed using the Okada (1985) model.

This model revealed a very gentle dip angle of N1 sliding surface of about $15 \pm 5^\circ$. Note that the optimal dip angles of dikes from the Model 1 remained fixed after the normal fault was added. This is because the normal fault, with a gentle dip angle, contributes little to the observed vertical displacements. In this case the total volume of the injected magma is $3.6 \times 10^6 \text{ m}^3$, the maximum opening of dikes is 3.2 m and the maximum slip is 0.7 m (Table 2, Fig. 17). This model better reproduces deformation along A–B and C–D profiles with the standard deviation of residuals of 2.4 and 1.5 cm for vertical

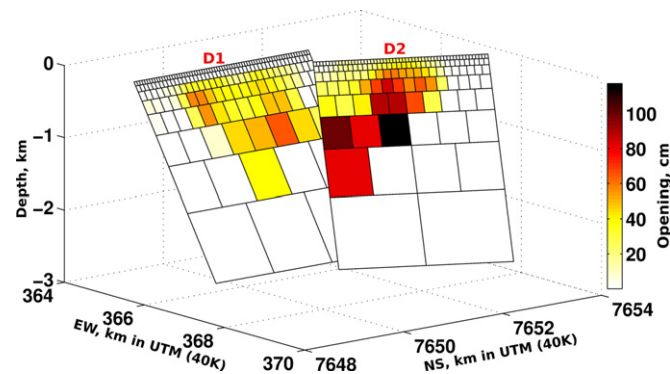


Fig. 11. Model 1 (two dikes D1–D2, opening only): distributed dike model, which surface locations are shown in Fig. 10 (d).

Table 3

Horizontal east-west (EW) and vertical (UD) correlation (COR) and root-mean-square error (RMS) for two profiles A–B and C–D for models 1–3 from Figs. 10–17.

Model, profile	EW COR	EW RMS, cm	UD COR	UD RMS, cm
Model 1, A–B	0.96	9.9	0.99	1.3
Model 1, C–D	0.95	4.5	0.98	1.5
Model 2, A–B	0.99	1.7	0.98	4.4
Model 2, C–D	0.97	1.8	0.95	3.7
Model 3, A–B	0.99	3.4	0.98	2.4
Model 3, C–D	0.98	2.3	0.98	1.5

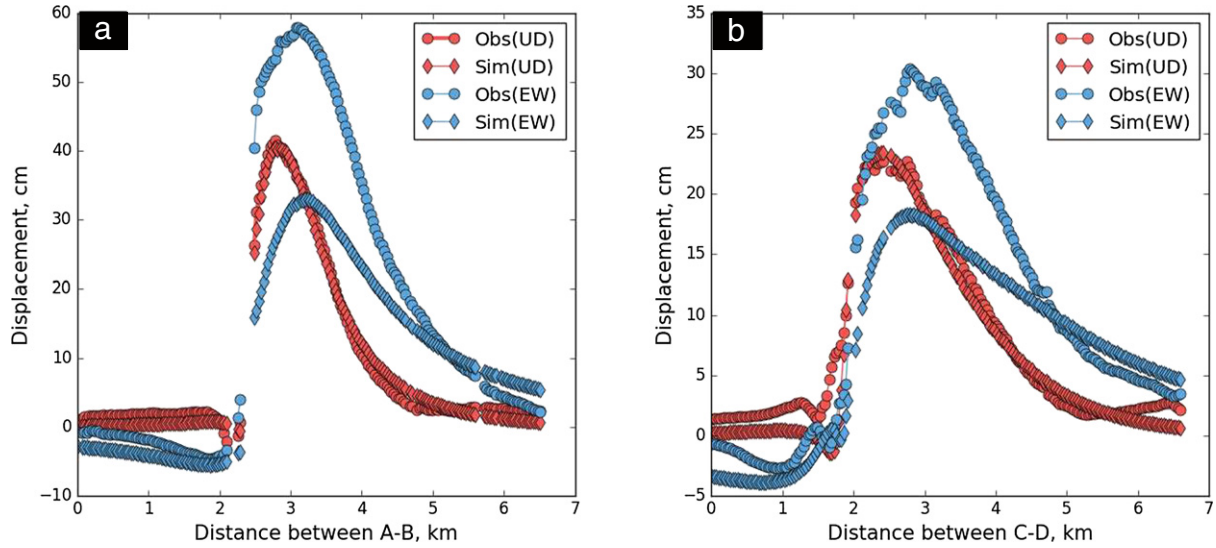


Fig. 12. Model 1 (two dikes D1–D2, opening only): comparison between observed and predicted deformation along two profiles A-B and C-D as shown in Fig. 10 (a).

component and 3.4 and 2.3 cm for horizontal east-west component, respectively (Table 3, Fig. 18). Residuals are distributed in the vicinity of the surface traces of the dikes and normal fault, which could be due to either the geometric complexity of the models or some other small-scale volcanic activities. The quality of fit depending on the selection of dip angles is shown in Fig. 18 (c,d). The largest opening on D1 is observed at about 1 km depth, the largest opening on D2 is

at about 0.5 km, and the largest slip on N1 is above 0.2 km (Fig. 18 (e,f)).

7. Discussion and conclusions

Modern Synthetic Aperture Radar satellites (e.g. RADARSAT-2, ALOS-2, Sentinel-1) provide very large volumes of SAR data that no

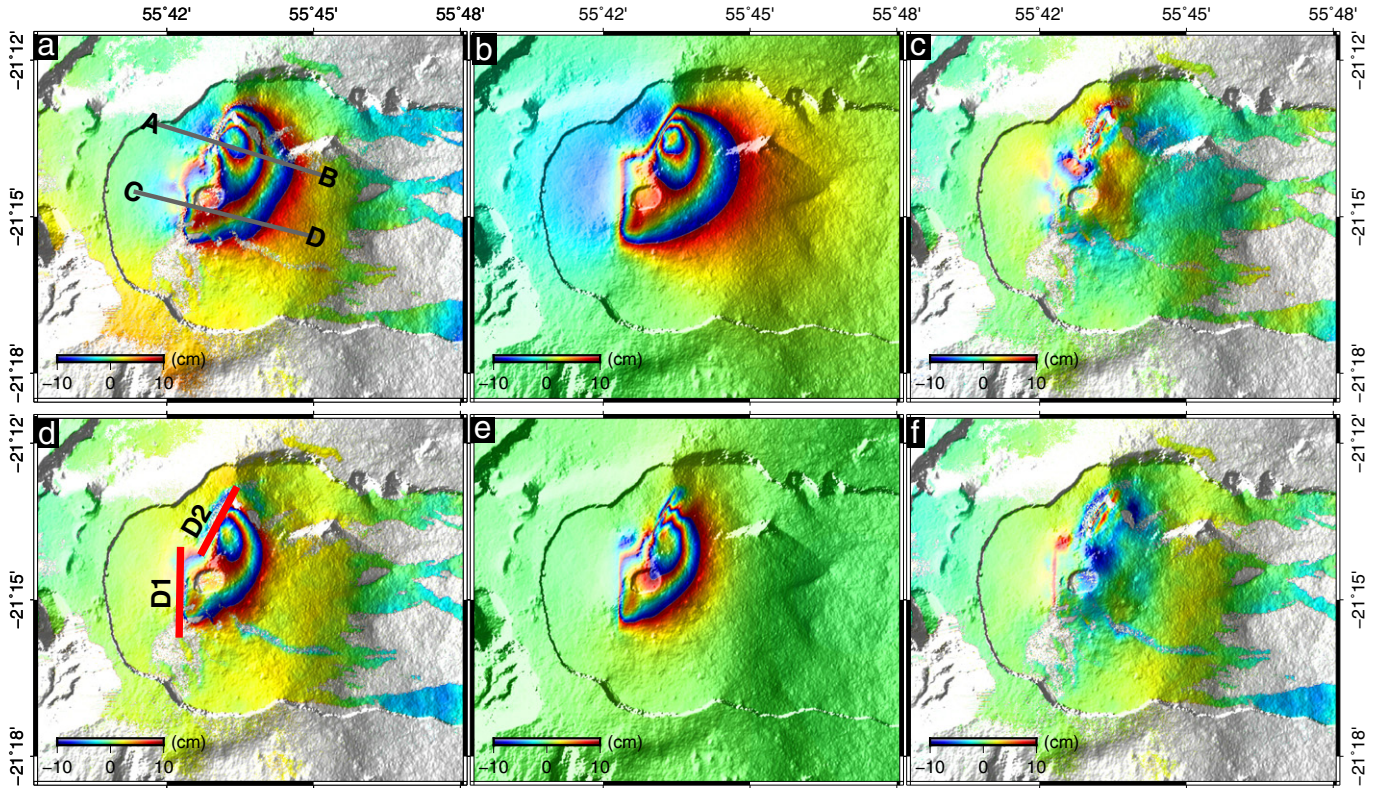


Fig. 13. Model 2 (two dikes D1–D2, opening and slip): horizontal east-west observed, modeled and residual deformation occurred during 20150619–20160109 (top row, a–c) and vertical observed, modeled and residual deformation during same time (bottom row, d–f). D1 and D2 are locations of modeled dikes at surface. A–B and C–D are profiles used for evaluating quality of modeling.

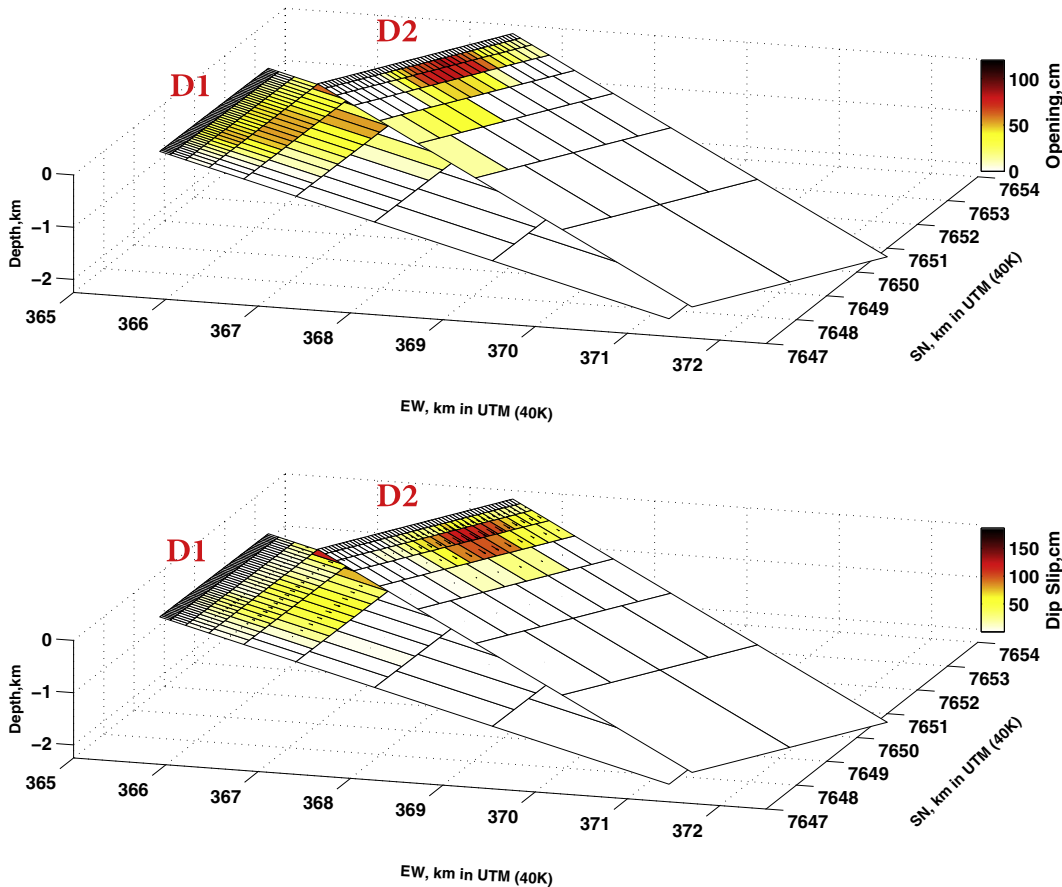


Fig. 14. Model 2 (two dikes D1–D2, opening and slip): distributed dike models (opening and slip), which surface locations are shown in Fig. 13 (d).

longer can be effectively and efficiently processed and interpreted manually. The development of novel automatic processing methodologies is warranted in order to fully utilize big data. Presented here, the MSBAS methodology is an example of a semi-automatic processing system for computing temporally dense two-dimensional

time series of surface displacement by combining multiple ascending and descending SAR data. The system is semi-automatic because it requires manual selection of the optimal processing parameters but after these parameters are selected, automatic processing can be applied to the consecutive acquisitions. The MSBAS is particularly

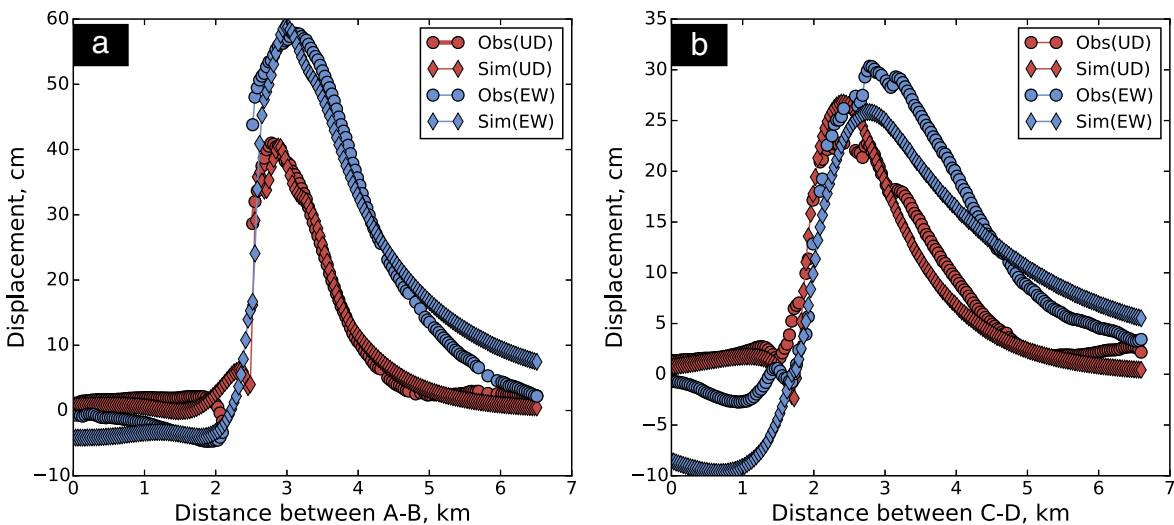


Fig. 15. Model 2 (two dikes D1–D2, opening and slip): comparison between observed and predicted deformation along two profiles A-B and C-D as shown in Fig. 13 (a).

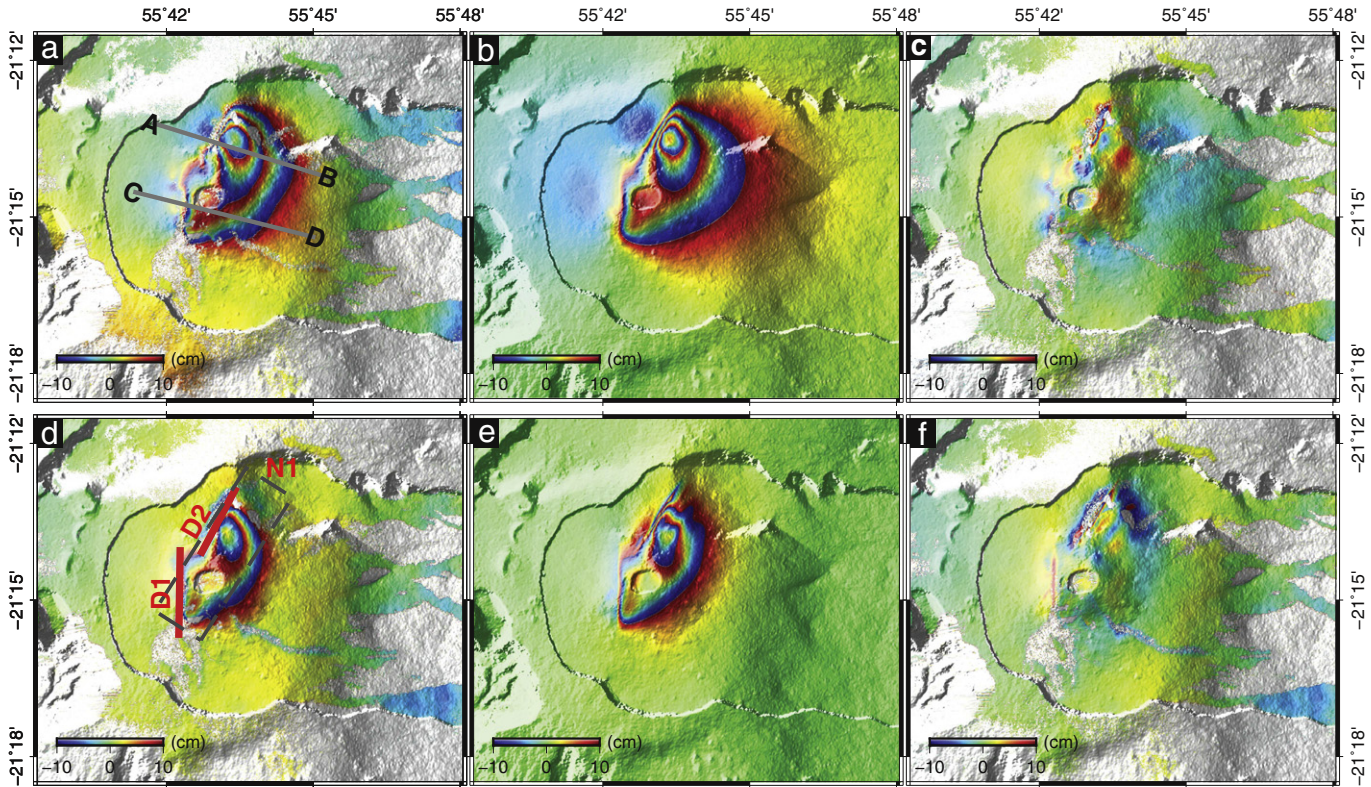


Fig. 16. Model 3 (two dikes D1–D2 opening only and normal fault N1 slip): horizontal east-west observed, modeled and residual deformation occurred during 20150619–20160109 (top row, a–c) and vertical observed, modeled and residual deformation during same time (bottom row, d–f). D1 and D2 are locations of modeled dikes at surface, gray dashed line shows location of normal fault N1. A-B and C-D are profiles used for evaluating quality of modeling.

suit for the near real time analysis: as soon as a new SAR data is acquired, it only requires to process the DInSAR deformation maps with the compatible pairing archives (based on the threshold temporal and spatial baseline values). Only a few new LOS deformation maps are then added to the MSBAS input and the reprocessing of the 2D time series and 2D deformation maps takes only a few minutes or tens of minutes, depending on the computer characteristics and the amount and the resolution of input data. The MSBAS has been utilized in various environments for mapping ground deformation due to mining, urban development, carbon sequestration, permafrost aggradation and pingo growth, and volcanic activity. By combining SAR data from various sensors the near real-time mapping can be achieved with high spatial resolution and over large areas, complementing the Global Navigation Satellite System (GNSS) and ground-based measurements.

Some challenges remain, including robust removal of atmospheric noise and residual orbital ramps and atmospheric noise. The atmospheric noise is particularly significant in the case of volcano monitoring as the large topographic relief, common to volcanic regions, produces non-linear disturbances that cannot be easily described, modeled and removed. Better understanding of theoretical and/or empirical relationships describing atmospheric noise in DInSAR data is required. Utilization of other kinds of remote sensing data and weather simulations is a promising approach actively developing (e.g. Li et al., 2005; Samsonov et al., 2014d; Bekaert et al., 2015). As the determination of satellite location becomes more accurate, the residual orbital component becomes smaller. Regularization implemented in MSBAS reduces the magnitude of noise but also introduces lag, similar to other smoothing algorithms. Lagging of DInSAR relative to GNSS can be observed, as in Fig. 8.

Because of the regularization-produced lag, near-real time monitoring can be challenging. The strength of regularization can be reduced if atmospherically corrected data is used instead, removing or reducing lag. More frequent SAR data acquisition also will reduce lag.

Phase decorrelation is probably the most significant limitation of DInSAR. It is caused by large changes in scattering characteristics between master and slave acquisitions. In volcano monitoring, phase decorrelation is usually caused by temporal changes (e.g. seasonal snow), surface changes (e.g. landslides, lahars, lava flows), and vegetation. Large gradients (i.e. large deformation over small spatial scales) that sometimes can be produced by volcanic activities that also cannot be detected by DInSAR, as observed near site DSRG in June 2014 (Fig. 8). Near-polar satellite acquisition geometry is insensitive to north-south motion. In the case of very large deformation in the range and azimuth directions, speckle tracking (Strozzi et al., 2002) or multi-aperture interferometry (Bechor and single, 2006) can be applied, but their precision is not sufficient for mapping transient deformation.

At Piton de la Fournaise the 2014–2015 period has been marked by the renewal of eruptive activity. As usually observed at Piton de la Fournaise, each eruption is preceded by a long-term cm-level ground deformation caused by magma pressurization at depth and by short-term dm-level ground deformation caused by dike injection to the surface (Peltier et al., 2016). Over 60 cm of horizontal and over 30 cm of vertical ground deformation was observed during the June 2014–October 2015 period produced by five eruptions. Large ground deformation recorded during the few minutes/hours-long dike injection are well detected both by GNSS and DInSAR. GNSS data processed in kinematic mode (one solution per epoch) shows

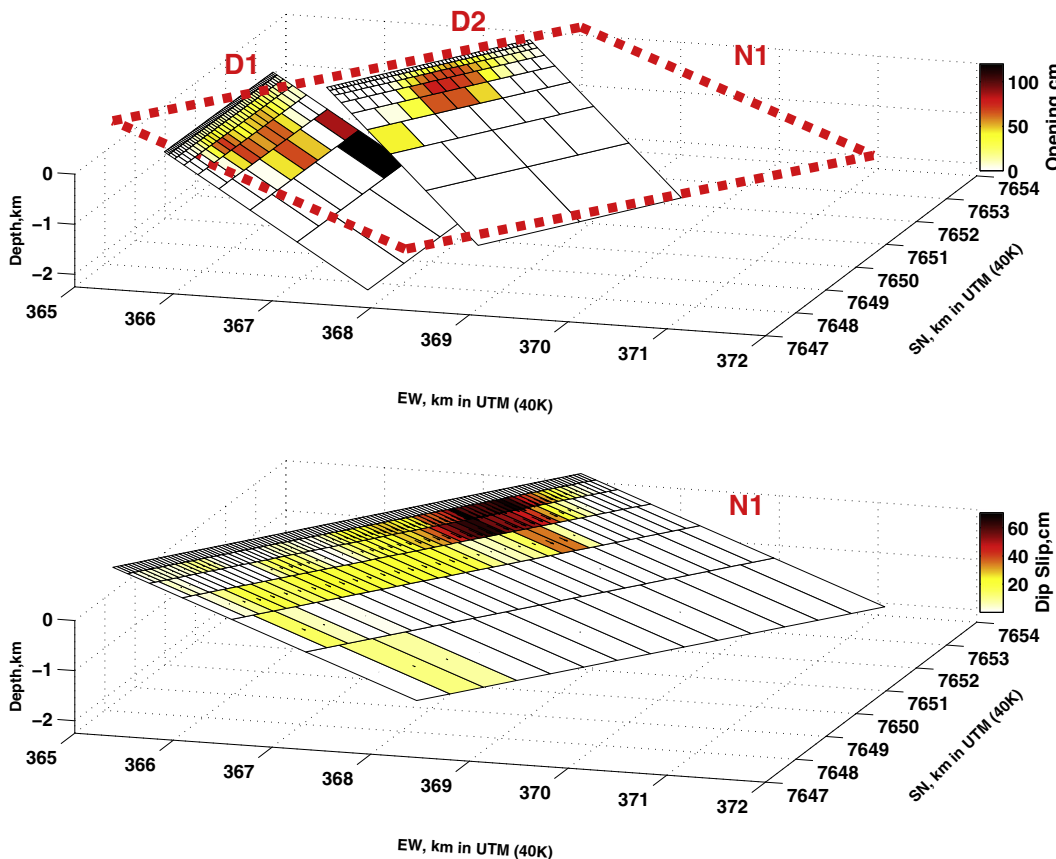


Fig. 17. Model 3 (two dikes D1–D2 opening only and normal fault N1 slip): distributed dike model, which surface locations are shown in Fig. 16 (d). Motion along normal fault outlined with red dashed line is shown in separate plot for clarity.

that these strong displacements are fast and occur in a few minutes/hours, i.e. the duration of the dike injection. MSBAS-derived time series confirm GNSS observations but with some lag introduced by regularization.

The ability of MSBAS to decompose line-of-sight deformation detected by DInSAR into horizontal east-west and vertical components is employed here to map surface deformation at Piton de la Fournaise in two dimensions. We observed that magnitude of horizontal component of ground deformation during 2014–2015 eruptions was nearly two times larger than the magnitude of vertical component (about 60 cm vs about 30 cm). Attempting to explain observed ground deformation we constructed three models of increased complexity. We demonstrated that simple opening of two dikes cannot describe observed ground deformation, particularly excessive horizontal east-west motion. To mitigate this effect we allowed dip-slip on two dikes, which described observed deformation well but produced shallow-dipping dikes, contradicting models of previous eruptions. In the final model we introduced, in addition to two dikes a shallow normal fault that accounted for the residual horizontal east-west motion observed in the first model. We demonstrated that the simple elastic model consisting of two dikes and a sliding surface can account for the observed ground deformation. Contribution of a horizontal structure (sill, fault, decollement) to the rapid deformation accompanying dike injection at Piton de la Fournaise has previously been suggested (e.g. Chaput et al., 2014; Tridon et al., 2016).

Permanent GNSS and tiltmeter stations installed in the field show that for each eruption the magma propagated first vertically below the volcano summit (during few to few tenths of minutes) then laterally around 1–1.5 km depth (Peltier et al., 2008; Peltier et al., 2009; Fukushima et al., 2010). This change in direction indicates a level of neutral buoyancy (Peltier et al., 2009; Fukushima et al., 2010) and explains why the further vertical migration cannot be caught by the DInSAR signals (Fukushima et al., 2010). Dips of the modeled dikes at Piton de la Fournaise are often oriented to the east with low values comprised between 50 and 70° (e.g. Peltier et al., 2008; Fukushima et al., 2005; Fukushima et al., 2010), producing the asymmetrical pattern of the ground deformation with a preferential motion of the eastern flank. Model 2, with dikes dipping 24–30° is thus not realistic because the roots of the dikes in this case are far from the summit and the reservoir. Even that observed deformation favors dikes dipping to the east when inverting geodetic data using simple elastic models, it is not necessarily representative of the reality. Indeed, by taking into account a more realistic elasto-plastic medium, Got et al. (2013) showed that a vertical dike could be associated with such asymmetrical pattern.

In Fukushima et al. (2010), the authors modeled via DInSAR data inversion the dike feeding of the five eruptions during the 1998–2000 period. They found that volume change for these five dikes represented 17% of the total volume of lava emitted to the surface during this period. This value is consistent with the ratio “dike volume vs emitted volume” found for the 2004–2005 eruptions (3.5 to

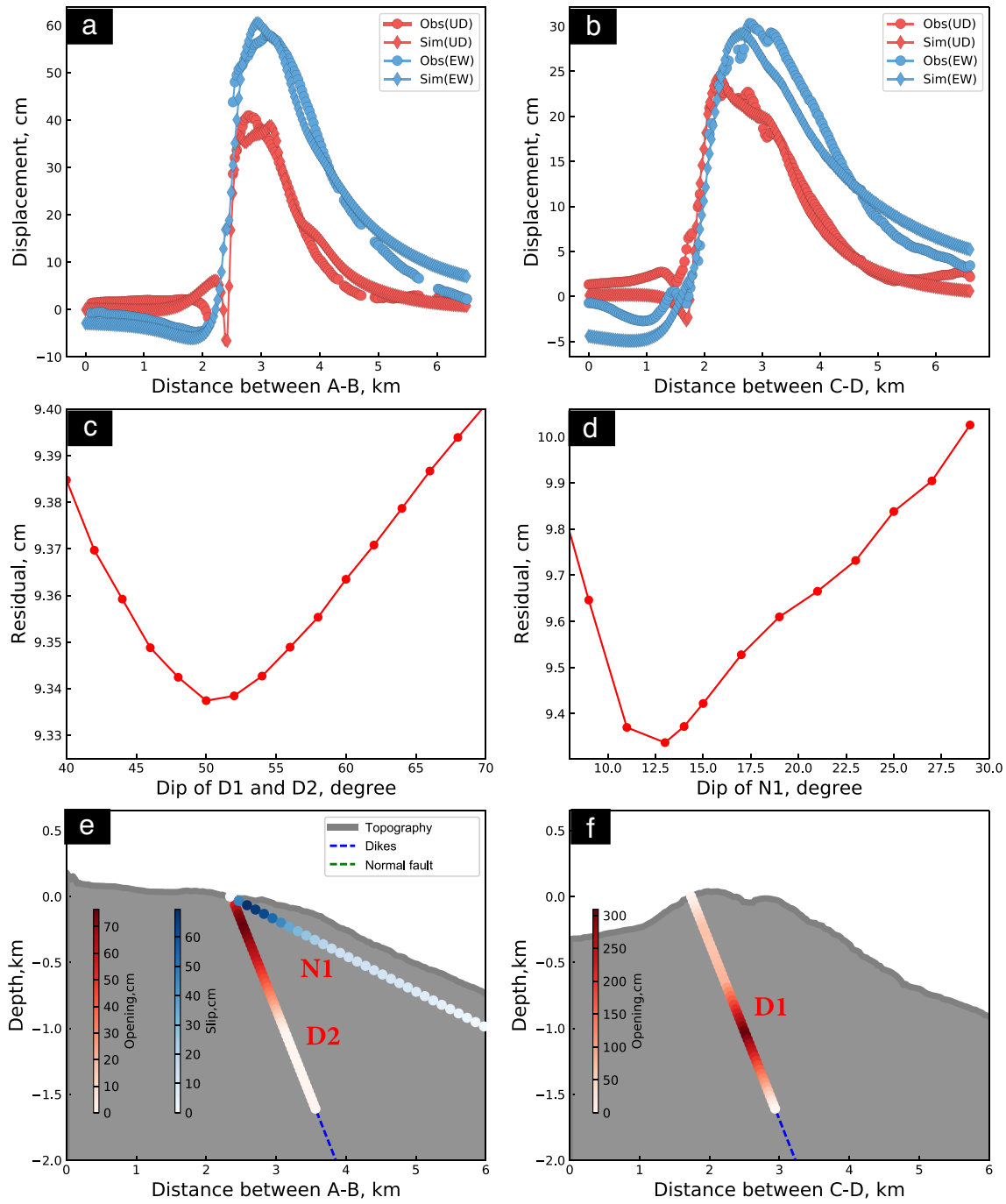


Fig. 18. Model 3 (two dikes D1–D2 opening only and normal fault N1 slip): comparison between observed and predicted deformation along two profiles (1-b) as shown in Fig. 16 (a). Dependence of root-mean-square error on dip angles for dikes D1–D2 (c) and normal fault N1 (d). Schematics of topography, dikes and normal fault along profiles A-B (e) and C-D (f).

68% depending of the eruptions, with a mean of 24%). Our preferred model shows volume change about 10% of the emitted volume. This confirms that most of the volcano growing is exogenous as previously observed (e.g. Fukushima et al., 2010; Peltier et al., 2012).

Acknowledgments

We thank the Canadian Space Agency (CSA) for providing RADARSAT-2 data. Figures were plotted with GMT and Gnuplot software and statistical analysis was performed with R software. This is

IPGP contribution 3841. The work of Dr. Tiampo was supported by funding from CIRES.

References

- Bachèlery, P., 1981. Le Piton De La Fournaise (Île De La Réunion). Etude Volcanologique Structurale. PhD thesis, Université de Clermont Ferrand.
- Bechor, N., Zeber, H., 2006. Measuring two-dimensional movements using a InSAR pair. Geophys. Res. Lett. 33, <http://dx.doi.org/10.1029/2006GL026883>.
- Bekaert, D.P.S., Walters, R.J., Wright, T.J., Hooper, A.J., Parker, D.J., 2015. Statistical comparison of InSAR tropospheric correction techniques. Remote Sens. Environ. 170, 40–47. <http://dx.doi.org/10.1016/j.rse.2015.08.035>.

- Chaput, M., Pinel, V., Famin, V., Michon, L., Froger, J.-L., 2014. Cointrusive shear displacement by sill intrusion in a detachment: a numerical approach. *Geophys. Res. Lett.* 41, 1937–1943. <http://dx.doi.org/10.1002/2013GL058813>.
- Cianetti, S., Giunchi, C., Casarotti, E., 2012. Volcanic deformation and flank instability due to magmatic sources and frictional rheology: the case of Mount Etna. *Geophys. J. Int.* 191 (3), 939–953. <http://dx.doi.org/10.1111/j.1365-246x.2012.05689.x>.
- Constantini, M., 1998. A novel phase unwrapping method based on network programming. *IEEE Trans. Geosci. Remote Sens.* 36 (3), 813–821.
- Czarnogorska, M., Samsonov, S., White, D., 2016. Airborne and spaceborne remote sensing characterization for Aquistore carbon capture and storage site. *Can. J. Remote. Sens.* <http://dx.doi.org/10.1080/07038992.2016.1171131>.
- Day, S.J., Carracedo, J.C., Guillou, H., Gravestock, P., 1999. Recent structural evolution of the Cumbre Vieja volcano, La Palma, Canary Islands: volcanic rift zone reconfiguration as a precursor to volcano flank instability? *J. Volcanol. Geotherm. Res.* 94 (1–4), 135–167. [http://dx.doi.org/10.1016/S0377-0273\(99\)00101-8](http://dx.doi.org/10.1016/S0377-0273(99)00101-8).
- Denlinger, R.P., Morgan, J.K., 2014. Characteristics of Hawaiian Volcanoes, Chapter Instability of Hawaiian Volcanoes. U.S. Geological Survey Professional Paper 1801, pp. 149–176.
- Dzurisic, D., 2006. *Geodetic Monitoring Techniques*. Springer.
- Feng, W., Li, Z., Hoey, T., Zhang, Y., Wang, R., Samsonov, S., Li, Y., Xu, Z., 2014. Patterns and mechanisms of coseismic and postseismic slips of the 2011 MW 7.1 Van (Turkey) earthquake revealed by multi-platform synthetic aperture radar interferometry. *Tectonophysics* 632, 188–198. <http://dx.doi.org/10.1016/j.tecto.2014.06.011>.
- Fournier, T., Pritchard, M., Finnegan, N., 2011. Accounting for atmospheric delays in InSAR data in a search for long-wavelength deformation in South America. *IEEE Trans. Geosci. Remote Sens.* 49 (10), 3856–3867. <http://dx.doi.org/10.1109/TGRS.2011.2139217>.
- Froger, J.-L., Fukushima, Y., Briole, P., Staudacher, T., Souriot, T., Villeneuve, N., 2004. The deformation field of the August 2003 eruption at Piton de La Fournaise, Reunion Island, mapped by ASAR interferometry. *Geophys. Res. Lett.* 31 (14). <http://dx.doi.org/10.1029/2004gl020479>. *Geophysical Research Letters*, 31(14), 2004. doi: 10.1029/2004GL020479.
- Fukushima, Y., Cayol, V., Durand, P., 2005. Finding realistic dike models from interferometric synthetic aperture radar data: the February 2000 eruption at Piton de La Fournaise. *J. Geophys. Res.* 110 (B03206). <http://dx.doi.org/10.1029/2004JB003268>.
- Fukushima, Y., Cayol, V., Durand, P., Massonnet, D., 2010. Evolution of magma conduits during the 1998–2000 eruptions of Piton de la Fournaise volcano, Réunion Island. *J. Geophys. Res.* 115 (B10). <http://dx.doi.org/10.1029/2009JB007023>.
- Goldstein, R., Werner, C., 1998. Radar interferogram filtering for geophysical applications. *Geophys. Res. Lett.* 25 (21), 4035–4038.
- Got, J.L., Peltier, A., Staudacher, T., Kowalski, P., Boissier, P., 2013. Edifice strength and magma transfer modulation at Piton de la Fournaise volcano. *J. Geophys. Res. Solid Earth* 118 (9), 5040–5057. <http://dx.doi.org/10.1002/jgrb.50350>.
- Griffiths, R., 2000. The dynamics of lava flows. *Annu. Rev. Fluid Mech.* 32, 477–518. <http://dx.doi.org/10.1146/annurev.fluid.32.1.477>.
- Hansen, P., O'Leary, D., 1993. The use of the L-curve in the regularization of discrete ill-posed problems. *SIAM J. Sci. Comput.* 14 (6), 1487–1503.
- Hansen, R., Fejt, A., 1996. A first quantitative evaluation of atmospheric effects on SAR interferometry. *Proceedings of the Fringe 96 Workshop*, Zurich, Switzerland.
- Herring, T.A., King, R.W., McClusky, S.C., 2010. GPS analysis at MIT, Release 10.4. Technical Report, Massachusetts Institute of Technology, Cambridge.
- Hooper, A., Bekaert, D., Spaans, K., Arkan, M., 2012. Recent advances in SAR interferometry time series analysis for measuring crustal deformation. *Tectonophysics* 514–517, 1–13. <http://dx.doi.org/10.1016/j.tecto.2011.10.013>.
- Lengliné, O., Duputel, Z., Ferrazzini, V., 2016. Uncovering the hidden signature of a magmatic recharge at Piton de la Fournaise volcano using small earthquakes. *Geophys. Res. Lett.* 43, <http://dx.doi.org/10.1002/2016GL068383>.
- Li, Z., Muller, J.P., Cross, P., Fielding, E.J., 2005. Interferometric synthetic aperture radar (InSAR) atmospheric correction: GPS, Moderate Resolution Imaging Spectroradiometer (MODIS), and InSAR integration. *J. Geophys. Res.* 110 (B03410).
- Lundgren, P., Kiryukhin, A., Millilo, P., Samsonov, S., 2015a. Dike model for the 2012–2013 Tolbachik eruption constrained by satellite radar interferometry observations. *J. Volcanol. Geotherm. Res.* 307, 79–88. <http://dx.doi.org/10.1016/j.jvolgeores.2015.05.011>.
- Lundgren, P., Samsonov, S., Lpez, Velez, Ordoez, M., 2015b. Deep source model for Nevado del Ruiz Volcano, Colombia, constrained by interferometric synthetic aperture radar observations. *Geophys. Res. Lett.* 42 (12), 4816–4823. <http://dx.doi.org/10.1002/2015GL063858>.
- Massonnet, D., Feigl, K., 1998. Radar interferometry and its application to changes in the Earth's surface. *Rev. Geophys.* 36 (4), 441–500.
- Mogi, K., 1958. Relations between the eruptions of various volcanoes and the deformation of the ground surfaces above them. *Univ. Tokyo Earthq. Res. Institute Bulletin* 36 (2), 99–134.
- Okada, Y., 1985. Surface deformation due to shear and tensile faults in a half-space. *Bull. Seismol. Soc. Am.* 75 (4), 1135–1154.
- Parker, R., 1994. *Geophysical Inverse Theory*. Princeton University Press.
- Peltier, A., Famin, V., Bachèlery, P., Cayol, V., Fukushima, Y., Staudacher, T., 2008. Cyclic magma storages and transfers at Piton de La Fournaise volcano (La Réunion hotspot) inferred from deformation and geochemical data. *Earth Planet. Sci. Lett.* 270 (3–4), 180–188. <http://dx.doi.org/10.1016/j.epsl.2008.02.042>. *Earth and Planetary Science Letters*, 270(3–4):180188, 2008. doi: 10.1016/j.epsl.2008.02.042.
- Peltier, A., Bachèlery, P., Staudacher, T., 2009. Magma transfer and storage at Piton de la Fournaise (La Réunion Island) between 1972 and 2007: a review of geophysical and geochemical data. *J. Volcanol. Geotherm. Res.* 184, 93–108. <http://dx.doi.org/10.1016/j.jvolgeores.2008.12.008>.
- Peltier, A., Bachèlery, P., Finizola, A., 2012. Internal structures and building of basaltic shield volcanoes: the example of the Piton de La Fournaise terminal cone (La Réunion). *Bulletin of Volcanology* 74, 1881–1897. <http://dx.doi.org/10.1007/s00445-012-0636-7>.
- Peltier, A., Beauducel, F., Villeneuve, N., Ferrazzini, V., Di Muri, A., Aiuppa, A., Derrien, A., Jourde, K., Taisne, B., 2016. Deep fluid transfer evidenced by surface deformation during the 2014–2015 unrest at Piton de la Fournaise volcano. *J. Volcanol. Geotherm. Res.* 321, 140–148. <http://dx.doi.org/10.1016/j.jvolgeores.2016.04.031>.
- Peltier, A., Froger, J.L., Villeneuve, N., Catry, T., 2017. Assessing the reliability and consistency of InSAR and GNSS data for retrieving 3D displacement rapid changes, the example of the 2015 Piton de la Fournaise eruptions. *J. Volcanol. Geotherm. Res.* <http://dx.doi.org/https://doi.org/10.1016/j.jvolgeores.2017.03.027>.
- Rosen, P., Hensley, P., Jougin, I., Li, F., Madsen, S., Rodriguez, E., Goldstein, R., 2000. Synthetic aperture radar interferometry. *Proc. IEEE* 88 (3), 333–382.
- Roult, G., Peltier, A., Taisne, B., Staudacher, T., Ferrazzini, V., Di Muro, A., 2012. A new comprehensive classification of the Piton de la Fournaise activity spanning the 1985–2010 period. Search and analysis of short-term precursors from a broad-band seismological station. *J. Volcanol. Geotherm. Res.* 241–242, 78–104.
- Samsonov, S., 2010. Topographic correction for ALOS PALSAR interferometry. *IEEE Trans. Geosci. Remote Sens.* 48 (7), 3020–3027.
- Samsonov, S., d'Oreye, N., 2012. Multidimensional time series analysis of ground deformation from multiple InSAR data sets applied to Virunga Volcanic Province. *Geophys. J. Int.* 191 (3), 1095–1108. <http://dx.doi.org/10.1111/j.1365-246x.2012.05669.x>.
- Samsonov, S., Beavan, J., Gonzalez, P., Tiampo, K., Fernandez, J., 2011a. Ground deformation in the Taupo Volcanic Zone, New Zealand observed by ALOS PALSAR interferometry. *Geophys. J. Int.* 187 (1), 147–160.
- Samsonov, S., van der Kooij, M., Tiampo, K., 2011b. A simultaneous inversion for deformation rates and topographic errors of DInSAR data utilizing linear least square inversion technique. *Comput. Geosci.* 37 (8), 1083–1091.
- Samsonov, S., d'Oreye, N., Smets, B., 2013a. Ground deformation associated with post-mining activity at the French-German border revealed by novel InSAR time series method. *Int. J. Appl. Earth Obs. Geoinf.* 23, 142–154.
- Samsonov, S., Gonzalez, P., Tiampo, K., d'Oreye, N., 2013b. Methodology for spatio-temporal analysis of ground deformation occurring near Rice Lake (Saskatchewan) observed by RADARSAT-2 DInSAR during 2008–2011. *Can. J. Remote. Sens.* 39 (1), 27–33.
- Samsonov, S., d'Oreye, N., González, P., Tiampo, K., Ertolahti, L., Clague, J., 2014a. Rapidly accelerating subsidence in the Greater Vancouver region from two decades of ERS-ENVISAT-RADARSAT-2 DInSAR measurements. *Remote Sens. Environ.* 143 (5), 180–191. <http://dx.doi.org/10.1016/j.rse.2013.12.017>.
- Samsonov, S., Gonzalez, P., Tiampo, K., d'Oreye, N., 2014. Modeling of fast ground subsidence observed in southern Saskatchewan (Canada) during 2008–2011. *Nat. Hazards Earth Syst. Sci.* 14, 247–257. <http://dx.doi.org/10.5194/nhess-14-247-2014>.
- Samsonov, S., Czarnogorska, M., White, D., 2015. Satellite interferometry for high-precision detection of ground deformation at a carbon dioxide storage site. *Int. J. Greenhouse Gas Control* 42, 188–199. <http://dx.doi.org/10.1016/j.ijggc.2015.07.034>.
- Samsonov, S.V., Tiampo, K.F., Camacho, A.G., Fernández, J., González, P.J., 2014c. Spatiotemporal analysis and interpretation of 1993–2013 ground deformation at Campi Flegrei, Italy, observed by advanced DInSAR. *Geophys. Res. Lett.* 41 (17), 6101–6108. <http://dx.doi.org/10.1002/2014GL060595>.
- Samsonov, S.V., Trishchenko, P., Tiampo, K., González, P.J., Zhang, Y., Fernández, J., 2014b. Removal of systematic seasonal atmospheric signal from interferometric synthetic aperture radar ground deformation time series. *Geophys. Res. Lett.* 41 (17), 6123–6130. <http://dx.doi.org/10.1002/2014GL061307>.
- Samsonov, S.V., Lantz, T.C., Kokelj, S.V., Zhang, Y., 2016. Growth of a young pingo in the Canadian Arctic observed by RADARSAT-2 interferometric satellite radar. *Cryosphere* 10 (2), 799–810. <http://www.the-cryosphere.net/10/799/2016/>. <http://dx.doi.org/10.5194/tc-10-799-2016>.
- Smets, B., d'Oreye, N., Kervyn, F., Kervyn, M., Albino, F., Arellano, S., Bagalwa, M., Balagizi, C., Carn, S., Darrah, T., Fernandez, J., Galle, B., Gonzalez, P., Head, E., Karume, K., Kavotha, D., Lukaya, F., Mashagiro, N., Mavonga, G., Norman, P., Osodundu, E., Pallerio, J., Prieto, J., Samsonov, S., Syauswa, M., Tedesco, D., Tiampo, K., Wauthier, C., Yalire, M., 2014. Detailed multidisciplinary monitoring reveals pre- and co-eruptive signals at Nyamulagira volcano (North Kivu, Democratic Republic of Congo). *Bull. Volcanol.* 76:787, 1–35.
- Staudacher, T., Peltier, A., Ferrazzini, V., Di Muro, A., Boissier, P., Catherine, P., Kowalski, P., Lauret, F., Lebreton, J., 2015. Active Volcanoes of the Southwest Indian Ocean: Piton De La Fournaise and Karthala. *Active Volcanoes of the World*, Chapter Fifteen Years of Intense Eruptive Activity (1998–2013) at Piton de la Fournaise Volcano (La Réunion): A Review. Springer, Berlin, pp. 251–269. http://dx.doi.org/10.1007/978-3-642-31395-0_15.
- Strozzi, T., Luckman, A., Murray, T., Wegmüller, C.L., Werner, U., 2002. Glacier motion estimation using SAR offset-tracking procedures. *IEEE Trans. Geosci. Remote Sens.* 40 (11), 2384–2391. <http://dx.doi.org/10.1109/TGRS.2002.805079>.
- Tiampo, K.F., Fernandez, J., Jentsch, G., Charco, M., Rundle, J.B., 2004. Inverting for the parameters of a volcanic source using a genetic algorithm and a model for magmatic intrusion in elastic-gravitational layered earth models. *Computers and Geosciences* 30 (9), 985–1001.
- Tridon, M., Cayol, V., Froger, J.L., Augier, A., Bachler, P., 2016. Satellite geodesy: results, numerical modeling, inverse theory, volcanic hazards and risks, inversion, flank

- displacement, InSAR, thermal contraction. Inversion of coeval shear and normal stress of Piton de la Fournaise flank displacement 121 (11), 7846–7866. <http://dx.doi.org/10.1002/2016JB013330>.
- Wadge, G., Webley, P.W., James, I.N., Bingley, R., Dodson, A., Waugh, S., Veneboer, T., Puglisi, G., Mattia, M., Baker, D., Edwards, S.C., Edwards, S.J., Clarke, P.J., 2002. Atmospheric models, GPS and InSAR measurements of the tropospheric water vapour field over Mount Etna. *Geophys. Res. Lett.* 29 (19). <http://dx.doi.org/10.1029/2002GL015159>. 11-1–11-4, October.
- Ward, S.N., Barrientos, S.E., 1986. An inversion for slip distribution and fault shape from geodetic observations of the 1983, Borah Peak, Idaho, earthquake. *J. Geophys. Res. J. Geophys. Res.* 91, 4909–4919.
- Wegmüller, U., Werner, C., 1997. GAMMA SAR Processor and Interferometry Software. In the 3rd ERS Symposium on Space at the Service of Our Environment. Florence, Italy.
- Zebker, H., Rosen, P., Hensley, S., 1997. Atmospheric effects in interferometric synthetic aperture radar surface deformation and topographic maps. *J. Geophys. Res. Solid Earth* 102B4, 7547–7563. <http://dx.doi.org/10.1029/96JB03804>.